International Journal of Plasticity 190 (2025) 104344

Contents lists available at ScienceDirect

International Journal of Plasticity

journal homepage: www.elsevier.com/locate/ijplas

Zirconium δ-hydrides: Strain localisation, ratcheting, and fatigue crack propagation

Daniel J. Long [a,b,*], Thibaut Dessolier [a], T. Ben Britton [a,c], Stella Pedrazzini [a], Fionn P.E. Dunne [a]

[a] Department of Materials, Royal School of Mines, Imperial College London, UK
[b] Department of Engineering Science, University of Oxford, UK
[c] Department of Materials Engineering, The University of British Columbia, Vancouver, Canada

ARTICLE INFO

Keywords:
Thermomechanical fatigue
Zirconium hydride
Hydride precipitation
Precipitation strains
Geometrically necessary dislocations
Digital image correlation
Fatigue crack growth
Fracture
Embrittlement
Hydride ratcheting

ABSTRACT

As many nations commit to achieving Net Zero, many low carbon scenarios indicate that civil nuclear power generation and the economics thereof are set to play a vital role. To maximise nuclear reactor operation lifetimes, it is essential to develop mechanistic understanding of failure and degradation mechanisms in safety-critical components for increasingly holistic reactor design codes and standards. In this paper, advanced micromechanical testing with in situ digital image correlation is used in combination with crystal plasticity modelling to study various aspects of damage associated with δ hydride precipitates in Zircaloy-4 for reactor fuel cladding applications. Measurements of static and cyclic hydride precipitation strains demonstrate a discernible strain field directionality (associated with intragranular precipitation) which was not previously reported, while cyclic thermomechanical loads are shown to promote the cyclic accumulation of strain due to repeated precipitation and dissolution of hydrides (hydride strain ratcheting) for up to five cycles, leading to the development of networks of geometrically necessary dislocations. Using crystal plasticity finite element modelling of the volumetric expansion associated with hydride precipitation, the strain directionality phenomenon is shown to be linked with hydride morphology. Comparisons with experimental strain fields also suggest that hydride plasticity is an important consideration for damage accumulation during precipitation. Experimental measurements of short fatigue crack propagation through Zircaloy-4 microstructures containing hydrides reveal new crack propagation mechanisms including decohesion, which on average, lead to accelerated rates of crack growth. Twins and hydride precipitation therein are also implicated in even more damaging fatigue behaviour as fatigue cracks are provided a seemingly brittle and direct path for fracture, which was not previously reported in the literature.

1. Introduction

The in-service performance of zirconium fuel cladding materials is important when considering the lifetime of a water-based nuclear reactor core. Improved lifetime is necessary to maximise the burn-up of nuclear fuel, decrease waste, and inform nuclear reactor safety cases. One major concern for zirconium-based cladding materials is the formation of zirconium hydrides, which can

* Corresponding author.
E-mail address: daniel.long@eng.ox.ac.uk (D.J. Long).

https://doi.org/10.1016/j.ijplas.2025.104344
Received 5 September 2024; Received in revised form 23 March 2025;
Available online 24 April 2025

reduce the strength, toughness, and damage tolerance of thin components (which are often < 1 mm thick due to the neutronics of a core). Furthermore, as reactor operation demands are increased, e.g. through load-following, there will be increased thermo-mechanical cyclic loading. This means we need to understand and improve ultimate cyclic loading requirements in cladding materials. Whilst fatigue is of concern to the industry, many challenges are thermomechanical, in which just a few cycles can result in the precipitation and dissolution of hydrides, as well as the accumulation of local precipitation strains within the microstructure. The present work is also motivated by a major literature gap in understanding how hydrides influence fatigue crack growth (FCG), particularly within the stage I regime, which is relevant to the in-service performance of fuel cladding materials. Moreover, the issue of strain ratcheting in hydrided zirconium alloys subjected to reactor-relevant thermomechanical cyclic loading has been reported (Kerr, 2009; Honniball et al., 2021), but it is not yet known how this affects fuel cladding performance. This motivates the present study, in which experimental capabilities to measure hydride ratcheting strains are developed, as well as the development of an associated predictive capability based upon crystal plasticity finite element (CPFE) modelling for strain localisation predictions. This study on fatigue-related structural integrity of fuel cladding materials compliments and extends the understanding of delayed hydride cracking (DHC) (Huang and Jiang, 1994; Kim et al., 2006; Sunil et al., 2020), which is most relevant to dry storage of spent fuel rods (Hong et al., 2020) and in some instances, CANDU pressure tube design (Radu and Roth, 2012).

Early work by Wanhill et al. (1972) sought to study the influence of zirconium hydrides on fatigue in Zircaloy-2 at room temperature and at 300 °C under variable-tension and reversed torsion loading conditions. At room temperature and 300 °C, for samples containing various hydrogen contents, the authors found no statistical differences in fatigue life owing to their inability to measure FCG in the stage I regime, i.e., only stage II cracking was considered, which was also immeasurable due to rates of growth being too high. Nevertheless, post-deformation analyses of fracture surfaces highlighted substantial differences in behaviour at different temperatures and for different hydrogen concentrations. At room temperature, it was concluded that hydrogen content could have a significant effect on fatigue damage mechanisms, as samples containing 600 ppmw hydrogen exhibited up to 50 % less (ductile) fatigue damage than non-hydrided specimens, despite having completely fractured due to e.g., cleavage and decohesion mechanisms within hydrides and at hydride-matrix interfaces, respectively. At 300 °C however, no samples fractured completely, and similar cracking mechanisms were observed for hydrided and non-hydrided materials; fracture toughness was shown to be virtually unaffected by hydrogen content, which was attributed to enhanced matrix ductility and the ability of the material to cross-slip. In some instances, hydride precipitates were observed to accommodate matrix shear by undergoing plastic deformation. Recently, this observation was reinforced by CPFE modelling and high-resolution digital image correlation (HR-DIC) work presented by Liu et al. (2023), which showed multiple examples of cross-hydride slip transfer in Zircaloy-4 under monotonic tensile loading. Extruded 3D crystal plasticity representations based on 2D surface measurements of microstructure regions containing δ phase hydride packets were shown to capture slip transfer events reasonably well, and provided new insights into the mechanisms which promote these events, based on crystallographic alignment, etc. Wanhill et al. (1972) showed that while dislocation slip activity accommodated most deformation during fatigue, even at room temperature, hydride cleavage and void formation between hydride-matrix and hydride-twin or matrix-twin interfaces were also important factors, particularly for crack nucleation. Twins were implicated in several instances of crack nucleation, though the authors did not declare the origin(s) of the twin features or whether there were local hydride interactions. However, it is reasonable to assume that since void formation at matrix-twin interfaces has not been reported for non-hydrided zirconium alloys, only twin-induced hydride precipitation can lead to such effects.

Using in situ synchrotron X-ray diffraction to capture strain evolution in hydrides under monotonic load (in Zircaloy-2), Kerr et al. (2008) showed that in some instances, there are three key deformation regimes: (i) fully elastic behaviour, (ii) matrix post-yield elastic behaviour (corresponding to a reduced modulus due to plasticity in the matrix and load transfer to the hydride), and (iii) strain saturation in the hydride due to either hydride fracture, interface failure, i.e., decohesion, or plasticity within the hydride. Based on the work presented by Liu et al. (2023), and depending on the hydride crystal orientation with respect to the remote loading direction, it is possible that (iii) is linked with both hydride plasticity and successive fracture or decohesion. The implications of this for fatigue are clear; where the applied load is sufficient to initiate plasticity in the matrix and the onset of regime (ii), the cyclic accumulation of plastic strain local to the hydride may generate stresses sufficient to initiate regime (iii), beginning with plasticity within the hydride, ultimately leading to fracture. This mechanism can aid in understanding the increased levels of brittle fracture in hydrided samples (Wanhill et al., 1972). Garlea et al. (2010) showed that in $R = 0$ fatigue testing of as-received (non-hydrided) and hydrided Zircaloy-4, FCG rates were substantially higher in the stage II regime, leading to premature failure (compared with steady Paris regime behaviour for as-received material). Moreover, the fatigue 'starting' behaviour for hydrided samples showed that the SIF necessary to initiate fatigue cracking was almost an order of magnitude lower than that for non-hydrided Zircaloy-4; this is attributed to matrix-hydride interactions leading to localised matrix plasticity and hydride-induced crack initiation. Hydride precipitation within the as received α phase 'Widmanstätten' microstructures was predominantly intergranular. The authors reported that the corresponding fracture paths were controlled by this, unlike FCG in non-hydrided Zircaloy-4, which is mostly transgranular (Wan and Dunne, 2020). Li et al. (2019) also studied crack initiation and FCG in hydrided zirconium alloys. Without reinforcement from FCG rate data, results indicated that fatigue behaviour is strongly affected by the morphological orientation of hydrides with respect to the remote loading direction. Specifically, post-deformation electron micrographs of sample surfaces revealed that hydrides which are oriented orthogonally to the loading direction are particularly damaging due to (i) increased cracking, i.e., longitudinally along the hydride, and (ii) the increased potential for hydride-matrix decohesion. In a more recent study by the same authors (Li et al., 2022), the fatigue life reduction associated with hydride-reorientation (20 % radial, i.e., orthogonal to the loading direction) is quantified at around 33 %, which highlights the increasingly detrimental effect of hydrides in materials subjected to combined thermal and mechanical loads.

In a recent publication by Taherijam et al. (2023) and Zan et al. (2024), electron backscatter diffraction (EBSD) and CPFE modelling were used to quantify the effects of hydride precipitation (and subsequent dissolution) in the absence of external loads on the

hydrostatic stress states and local rotational fields, i.e., geometrically necessary dislocation (GND) density. Precipitation was shown to produce networks and discrete bands of GNDs which interconnect hydrides, with densities of up to 1000 μm^{-2} (with highest values near hydride tips); this disaccords with EBSD-based measurements from Birch et al. (2023), which show maximum GND densities of around 30 μm^{-2}. The hydrostatic stress states which develop upon dissolution, as predicted by Taherijam et al. (2023), were very large and tensile (up to 600 MPa) within the former hydride region. This indicates that reprecipitation is highly likely to occur within the same region, while various locations surrounding the original hydride were shown to develop both tensile and compressive hydrostatic stresses. The authors note that the GND networks produced initially are also likely to result in additional precipitation locally.

While multiple publications highlight the effects of high temperature environments on fatigue in hydrided zirconium alloys (Wanhill et al., 1972; Zhang et al., 2020; Cockeram and Kammenzind, 2018) and others the various hydrogen and strain ratcheting effects associated with thermal cycling (Eadie et al., 1993; Li et al., 2013; Chen et al., 2017), no studies have yet quantified the local stress or strain states associated with multi-cycle hydride precipitation, which is crucial for mechanistic understanding of failure and prediction thereof at microstructure length scales. This research paper, which is broadly experimental, addresses these literature gaps and is aimed at (i) quantifying local deformation levels due to hydride precipitation and subsequent ratcheting under cyclic thermomechanical loads, (ii) determining the various mechanisms (and the factors controlling these mechanisms) involved in short FCG in Zircaloy-4, and (iii) assessing the effects of hydride precipitates on local short FCG rates, aided by in situ digital image correlation (DIC).

2. Methods

2.1. Material

Samples for this work are manufactured from Zircaloy-4 rolled plate material in the as-received condition (from *Rolls-Royce plc.*). Samples are cut using a *Fanuc* wire electrical discharge machine (EDM) with a wire diameter of 120 μm. Notches are also machined using a single wire EDM pass. Generally, rolled plates of Zircaloy-4 are highly textured, leading to samples with either strong basal or prismatic textures (depending on how they are cut from the plate); samples used in this work are characterised by the latter. For the in situ DIC methodology used here, spatial resolution of the measured strain fields is limited to around 3 μm (the displacement field spatial resolution is around 1 μm). Hence, to maximise its potential for understanding the role of crystallography in deformation, a heat treatment is applied to each sample to generate very large, blocky α grains, the features of which can be easily resolved in situ. The heat treatment used here was developed by Tong (2016) and was designed to achieve very large grain growth. The samples were heated to 800 °C, which is just below the α-β transus temperature (the transus temperature is around 820 °C for Zircaloy-4 (Massih and Jernkvist, 2021)) and were held at this temperature for 336 h (14 days). To prevent oxidation during heat treatments, the samples were encapsulated in quartz tubing and backfilled with argon gas.

Following the grain growth heat treatment, an electrolytic hydrogen charging procedure was used to introduce hydrogen to the matrix and form hydride precipitates. An adaptation of the Lepage technique (Lepage et al., 1998) was adopted here, which involves the gradual diffusion of hydrogen into the material which creates a surface layer of hydride within the zirconium-rich matrix, using an electrolytic reaction. To improve reliability, the altered version of this technique, which was described by Birch et al. (2019), is used in this work (Birch et al., 2019 replaced Lepage's lead anode with platinum to prevent reaction poisoning). The electrochemical cell consists of the Zircaloy-4 acting as a cathode and a platinum mesh anode and these are both submerged in a sulphuric acid solution held at 65 ± 5 °C to increase the reaction rate. The circuit was completed with a potentiostat operating to provide a current density of 2 kA/m^2 (relative to the charged area of the sample) for 24 h. Prior to charging, each sample is ground to 2000 grit level, primarily to remove oxides and maintain consistency between samples. The sample was masked with an acrylic protective layer so that only a single surface is charged, such that measurements of the deposited hydride layer thickness can be made after charging; this is later used to assess the success of the procedure. Upon generating a sufficiently thick hydride layer (which is dependent upon sample thickness, sample volume, and desired hydrogen content and is assessed using an empirical model (Lepage et al., 1998), with a target concentration of 150 – 200 ppmw), a homogenisation heat treatment is used to uniformly distribute hydrogen, and hence hydrides throughout each sample. This procedure involves raising the sample temperature to a sufficient level to bring the hydrogen into solution (but below the β-transus temperature) and holding the sample at this temperature for some time to allow the hydrogen to diffuse until an equilibrium concentration is reached throughout. According to Lepage et al. (1998), samples should be held at 400 °C for 7 h to ensure a uniform hydride distribution at the mm length-scale. Homogenisation in Zircaloy-4 at this temperature was validated independently by McNamara (2014). To ensure the hydrogen was well dispersed throughout the sample, a longer heat treatment time was used here. For this heat treatment step, samples are encapsulated in quartz tubing in an inert environment to prevent high temperature oxidation.

Table 1
Sample surface preparation steps taken for polarised light microscopy. Samples are mounted in 30 mm diameter thermoset polymer cylinders.

Step	Abrasive / solution	Applied load (N)	Time (minutes)
Grinding	800 grit SiC abrasive pad	10	As required
	1200 grit SiC abrasive pad		4
	2000 grit SiC abrasive pad		8
	4000 grit SiC abrasive pad		16
Polishing	Colloidal silica suspension (0.04 μm particles)		30

For EBSD characterisation, a multi-step sample surface preparation procedure is adopted. The steps first taken for polarised light microscopy are listed in Table 1.

Beyond this, for improved electron backscatter pattern (EBSP) detection, an additional step of ion beam polishing using the *Gatan PECS II* system at cryogenic temperatures is used. Polishing conditions, which were optimised for Zircaloy-4 by Fang et al. (2022) are used here and are listed in Table 2.

In brief, ion beam polishing, specifically broad ion beam (BIB) polishing, uses highly energetic ions to sputter and remove material from the sample surface. It is a highly robust method which introduces significantly less surface damage than mechanical polishing, though it can cause low levels of surface radiation damage at high energy levels, which can promote hydride precipitation, particularly when samples are wet (Fang et al., 2022).

2.2. Micro-thermo-mechanical testing and digital image correlation

For studies of short fatigue crack propagation and thermomechanical ratcheting effects in hydrided Zircaloy-4, force-controlled three-point bending is used. As illustrated in Fig. 1(a), samples are notched at the centre to generate stress concentrations sufficient to initiate and propagate cracks within hundreds of cycles, and to ensure stress-driven hydrogen redistribution during thermo-mechanical testing. Prior to thermomechanical testing, a thermal gradient heat treatment is also applied to drive hydrogen away from regions with high residual stress, for reasons outlined in Appendix A. The $12 \times 3 \times 3$ mm^3 beam design enables samples to be easily mounted on stubs for electron imaging and EBSD characterisation both before and after testing. Notch geometry and applied load are used to tailor the notch tip stress (or equivalent stress intensity factor (SIF) for FCG) for each test. The notch tip SIF is calculated for samples in 3-point bending using the method reported by Wan and Dunne (2020). In situ DIC is performed across a region of interest local to the notch for each test. EBSD characterisation of the same region of interest enables linkage between micromechanical test data and microstructure and crystallography for mechanistic insights at the appropriate length-scale into factors which influence damage localisation and cracking.

2D-DIC analysis was performed using a single camera, as most deformation is confined to the plane of bending with a relatively small deflection. A digital camera (8 megapixel 12-bit *QIClick*) coupled with a long-range optical microscope (*Questar QM-100*) is used to image the front surface of each sample during testing, as shown in Fig. 1 (b). A fibreoptic illuminator is used to provide coaxial illumination of the sample. The image resolution, and hence DIC resolution is approximately 3 μm. For fatigue testing at high frequencies, a high sampling rate is required to ensure sufficient resolution when attempting to capture data at the peaks and troughs of each cycle; for example, for a test frequency of 0.1 Hz, a sampling rate of 1 Hz is used. The DIC speckle pattern applied to the surface of each sample should contain features measuring close to the DIC resolution. Here, a polishing solution from *Struers*, containing 1-micron single crystal diamond particles is used, and is applied as an aerosol. The diamond particles are suspended in an ethanol-based solution, most of which is removed by rinsing in acetone and drying after each spray. An optical microscope is used to carefully assess the pattern quality after each spray. According to *iDICs*' good practice guide for DIC (Bigger et al., 2018), pattern density should be around 50 %, i.e., 50 % of the sample surface area should be covered with diamond particles. After testing, surface micrographs containing the speckle patterns are processed using *Ncorr*, (Blaber et al., 2015) which is an open-source *Matlab*-based 2D-DIC program. From the displacement fields, the components of the deformation gradient are calculated using a separate code, according to Eq. (1), where x and y are the horizontal and vertical displacements, X and Y the horizontal and vertical measurements coordinates, and i and j the corresponding DIC row and column index points. The strain tensor is extracted using $\boldsymbol{\varepsilon} = \frac{1}{2}\left(\boldsymbol{F}^{\mathrm{T}}\boldsymbol{F} - \boldsymbol{I}\right)$.

$$
\begin{aligned}
F_{xx,i,j} &= 1 + \frac{x_{i,j+1} - x_{i,j-1}}{X_{i,j+1} - X_{i,j-1}} \\
F_{yy,i,j} &= 1 + \frac{y_{i+1,j} - y_{i-1,j}}{Y_{i+1,j} - Y_{i-1,j}} \\
F_{xy,i,j} &= \frac{x_{i+1,j} - x_{i-1,j}}{Y_{i+1,j} - Y_{i-1,j}} \\
F_{yx,i,j} &= \frac{y_{i,j+1} - y_{i,j-1}}{X_{i,j-1} - X_{i,j-1}}
\end{aligned}
\tag{1}
$$

For full-field measurements of GND density based on the displacement and deformation gradient fields, it is assumed that post-test residual deformation measured in the absence of external loads is entirely plastic (Jiang et al., 2016). Whilst this is not entirely true (as there are residual elastic strains), the total strains which are imposed on the matrix due to hydride precipitation are later shown to be substantial by comparison, to the extent that any residual elastic strains within the Zircaloy-4 matrix are likely to be of the same order as the experimental error, i.e., are negligible. This is a long-standing issue, particularly for fatigue crack nucleation problems in which the cyclic cumulative strain (and hence GND density evolution) is small. Nevertheless, a quantitative comparison of experimental stress distributions derived from this assumption CPFE modelling results was shown to yield excellent agreement in Zircaloy-4 (Liu

Table 2
Ion beam polishing parameters used for sample preparation for EBSD.

Incident polishing angle (°)	Ion energy (keV)	Sample temperature (°C)	Duration (minutes)
8	8	<−50	30

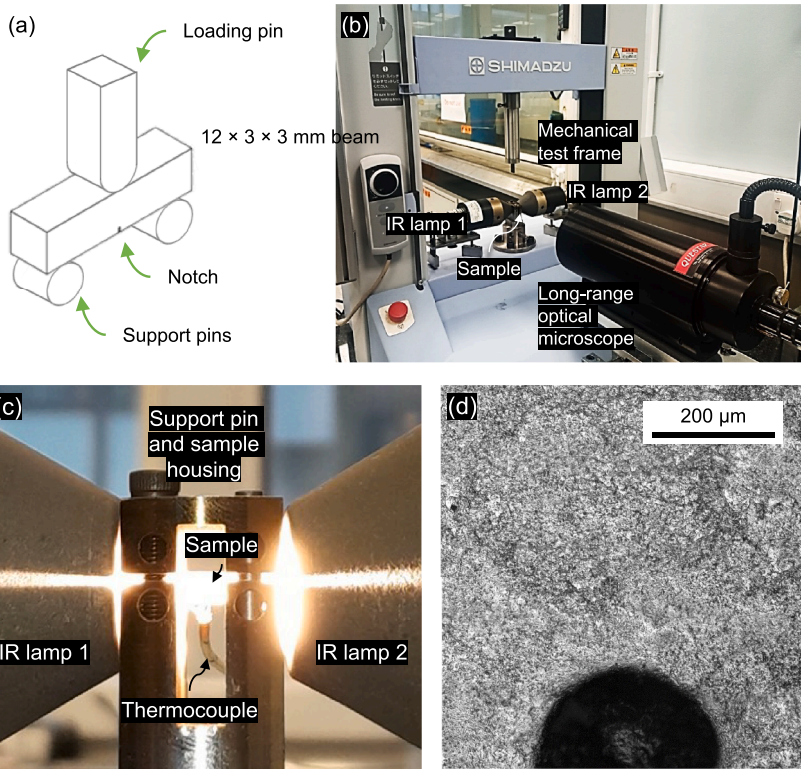

Fig. 1. (a) Illustration of three-point bending configuration. The notch, which is visible at the front surface, extends through the sample thickness (nominally 3 mm). Support pins are 3 mm in diameter and the loading pin tip radius is 1.5 mm. Spacing between support pins is 10 mm. Notch height and radius are approximately 300 μm and 100 μm, respectively. (b) Micro-thermo-mechanical test setup. Beam samples are placed on two horizontal support pins at the base of the 10 kN Shimadzu mechanical test frame; a screw-driven crosshead applies a downward load to the centre of the beam for three-point bending. Infrared lamps are positioned at either end of the beam for heating. The long-range optical microscope is positioned directly in front of the centre of the sample. (c) IR lamp configuration in heated and unloaded state (load pin is not in contact with sample). (d) Example of DIC speckle pattern in the vicinity of a notch.

et al., 2020). The deformation gradient in the unloaded state is then $\boldsymbol{F}^{\text{unload}} = \boldsymbol{F}^{\text{p}}$. Since the individual slip system contributions to plastic deformation are unknown in experiments, Ashby's analytical solution (Ashby, 1970) is generalised in 2D and is given by Eq. (2),

$$\boldsymbol{\rho}_{\text{GND}} = \rho_{\text{GND},k,l} = \frac{1}{b}\nabla \times \boldsymbol{F}^{\text{p}} = \frac{1}{b} \cdot \begin{bmatrix} \frac{\partial F^{\text{p}}_{xx}}{\partial x} & \frac{\partial F^{\text{p}}_{xx}}{\partial y} \\ \frac{\partial F^{\text{p}}_{yy}}{\partial x} & \frac{\partial F^{\text{p}}_{yy}}{\partial y} \\ \frac{\partial F^{\text{p}}_{xy}}{\partial x} & \frac{\partial F^{\text{p}}_{xy}}{\partial y} \\ \frac{\partial F^{\text{p}}_{yx}}{\partial x} & \frac{\partial F^{\text{p}}_{yx}}{\partial y} \end{bmatrix} \tag{2}$$

where b is the $<a>$ Burgers vector magnitude, assuming a negligible $\langle c+a \rangle$ pyramidal slip contribution. The spatial gradients of deformation gradient are determined in the same way as the components of deformation gradient are determined from the spatial gradients of displacement, e.g., $\frac{\partial F^{\text{p}}_{xx}}{\partial x}_{i,j} = \frac{F^{\text{p}}_{xx,\ i,j+1} - F^{\text{p}}_{xx,\ i,j-1}}{x_{i,j+1} - x_{i,j-1}}$. The scalar GND density is then given by taking the 2nd order norm of its components, which minimises the sum of the squares of dislocation densities.

$$\rho_{\text{GND}} = \sqrt{\sum_{l=1}^{2}\sum_{k=1}^{4} \rho^2_{\text{GND},k,l}} \tag{3}$$

This formulation is an adaptation of that reported by Xu et al. (2021), in which GND density was approximated as the curl of the plastic strain tensor, i.e., $\boldsymbol{\rho}_{\mathrm{GND}} = \frac{1}{b}\nabla \times \boldsymbol{\varepsilon}^{\mathrm{p}}$. Using the current revised formulation is more precise since the asymmetric rotation components are accounted for in full.

As shown in Fig. 1(c), air-cooled 250 W infrared (IR) lamps (from *Precision Control Systems ltd.*) are positioned at either end (3 × 3 mm ends) of the beam; this configuration was previously shown to provide reasonably uniform heating across the beam length (Poole, 2020). For temperature control, K-type thermocouples are spot-welded to the rear face of each beam, which feed into a full proportional-integral-derivative (PID) control loop. A *Eurotherm 2416* controller is used to control both the power provided to the lamps, and pneumatic solenoid valves which control air flow to the lamps. An air compressor with appropriate filtration is used to provide a steady flow of air at approximately 30 L/min per lamp.

2.3. Thermomechanical loading conditions and crystal plasticity finite element modelling

The constitutive framework of the crystal plasticity model implemented in this work makes use of Lee's multiplicative decomposition (Lee and Liu, 1968) of the deformation gradient from continuum mechanics, as shown in Eq. (4),

$$\boldsymbol{F} = \boldsymbol{F}^{\mathrm{e}}\boldsymbol{F}^{\mathrm{p}}\boldsymbol{F}^{\mathrm{th}} \tag{4}$$

where $\boldsymbol{F}^{\mathrm{e}}$ is the elastic deformation gradient and $\boldsymbol{F}^{\mathrm{th}} = \boldsymbol{I} + \Delta T\boldsymbol{\alpha}$ is the deformation gradient due to thermal expansion (ΔT is the change in temperature relative to the undeformed state and $\boldsymbol{\alpha}$ is a diagonal tensor with components corresponding to the HCP principal directions – see Table 3). Note that in subsequent sections, where eigenstrains due to hydride precipitation are considered, there is an additional deformation gradient contribution. Hence, Eq. (4) applies only to the Zircaloy-4 matrix. The elastic deformation gradient is used to determine the stress state via Hooke's Law and is given by inverting the plastic deformation gradient, $\boldsymbol{F}^{\mathrm{e}} = \boldsymbol{F}\boldsymbol{F}^{\mathrm{p}-1}\boldsymbol{F}^{\mathrm{th}-1}$. The elastic (Green) strain tensor is then simply $\boldsymbol{\varepsilon}^{\mathrm{e}} = \frac{1}{2}\left(\boldsymbol{F}^{\mathrm{e}\mathrm{T}}\boldsymbol{F}^{\mathrm{e}} - \boldsymbol{I}\right)$. In the current model, it is assumed that all plastic deformation in Zircaloy-4 is accommodated for by dislocation glide or slip, a process in which the application of a sufficiently large local shear stress results in dislocation motion. The following mechanistic slip rule (Dunne et al., 2007) is introduced to capture the rate of plastic shear on a given slip plane, *i*,

$$\dot{\gamma}^{i} = \rho_{\mathrm{m}}\omega b^{2}\exp\left(\frac{-\Delta F}{k_{\mathrm{B}}T}\right)\sinh\left(\frac{\left(\tau^{i} - \tau_{\mathrm{c}}^{i}\right)\Delta V}{k_{\mathrm{B}}T}\right) \tag{5}$$

where $\dot{\gamma}^{i}$ is the rate of plastic shear strain, ρ_{m} is mobile dislocation density, ω the frequency of attempts for dislocations to surmount thermal energy barriers, ΔF is activation energy, τ_{c}^{i} is critical resolved shear stress (CRSS) (and τ^{i} is applied shear stress for the corresponding slip system), ΔV is activation volume and k_{B} and T have their usual meanings. This slip rule originates from Gibbs' (Gibbs, 1964) statistical mechanics work on thermally activated escape of pinned dislocations. To glide, pinned dislocations must overcome thermal energy barriers presented by obstacles, the probability of which is controlled by the activation energy (or Helmholtz energy), ΔF; together with the frequency of 'jump' attempts, ν, and work done by the stress field, $\left(\tau^{i} - \tau_{\mathrm{c}}^{i}\right)\Delta V$, the rate of plastic shear can be determined. Activation energy and activation volume are also therefore the most important terms controlling strain-rate sensitivity of the material (Liu et al., 2020). Physically, the activation volume represents the volume of material involved in the thermally activated glide of a dislocation (Laplanche et al., 2018), and is therefore linked with the pinning distance, l (Dunne et al., 2007; Fleck and Hutchinson, 1993). Validation of these strain-rate sensitive terms was carried out using creep relaxation data at room and elevated

Table 3
Room temperature and temperature dependent anisotropic elastic properties and CRSS values for single crystal Zr alloys.

Property	Value at room temperature	Temperature dependent value (Liu et al., 2020)	Units
Anisotropic elastic properties			
E_1	98.308	$-0.0755T + 120.4411$	GPa
E_3	132.208	$-0.0372T + 132.8621$	GPa
G_{12}	32.010	$-0.0233T + 38.8367$	GPa
ν_{12}	0.4006	$3.4273 \times 10^{-4}T + 0.3002$	–
ν_{13}	0.2375	$-9.1182 \times 10^{-5}T + 0.2642$	–
Anisotropic thermal expansion coefficients (assumed constant) (Abdolvand, 2019)			
α_1	5.30×10^{-6}	–	K^{-1}
α_2	5.30×10^{-6}	–	K^{-1}
α_3	1.01×10^{-5}	–	K^{-1}
CRSS (plastic) values for Zr alloys (Gong et al., 2015)			
$\tau_{\mathrm{c},0}^{\mathrm{prism}}$	153	$26.3 \times \exp(514.7/T)$	MPa
$\tau_{\mathrm{c},0}^{\mathrm{basal}}$	203	$1.33\ \tau_{\mathrm{c},0}^{\mathrm{prism}}(T)$	MPa
$\tau_{\mathrm{c},0}^{\mathrm{pyramidal}\langle c+a\rangle}$	532	$3.48\ \tau_{\mathrm{c},0}^{\mathrm{prism}}(T)$	MPa

temperatures; hence, this modelling framework is ideally suited to the thermomechanical problems associated with hydride precipitation under reactor operating conditions. Note that Eq. (5) only applies where the applied shear stress applied over a given slip system is greater than the corresponding critical value; otherwise, $\dot{\gamma}^i = 0$. The contributions of individual slip systems to overall plastic strain are then accounted for within the plastic velocity gradient, $\boldsymbol{L}^{\mathrm{p}}$, which is calculated using Schmid's Law, as shown in Eq. (6).

$$\boldsymbol{L}^{\mathrm{p}} = \sum_{i=1}^{M} \left(\dot{\gamma}^i \boldsymbol{n}^i \otimes \boldsymbol{s}^i \right) \tag{6}$$

where M is the total number of slip systems and $\boldsymbol{n}^i$ and $\boldsymbol{s}^i$ represent the individual slip system normal and slip direction vectors, respectively. The $\otimes$ function represents the dyadic product of vectors $\boldsymbol{n}^i$ and $\boldsymbol{s}^i$, and produces a matrix. The plastic velocity gradient is then related back to the plastic deformation gradient by $\boldsymbol{L}^{\mathrm{p}} = \dot{\boldsymbol{F}}^{\mathrm{p}} \boldsymbol{F}^{\mathrm{p}-1}$. The various slip systems in Zircaloy-4 are illustrated in Fig. 2. In relation to the atomic crystallography of hexagonal close packed (HCP) materials; in the current paper, hydride dislocation slip is not considered. In later explicit representations of hydride stringers, they are modelled as continuous elastic features, based on room temperature property data following precipitation (Taylor, 1934; Fisher and Renken, 1964). The classic Taylor hardening model (Taylor, 1934) is used within the crystal plasticity framework to account for plastic strain hardening due to dislocations, as shown in Eq. (7),

$$\tau_{\mathrm{c}}^i = \tau_{\mathrm{c},0}^i + \mu b \sqrt{\rho_{\mathrm{SSD}} + \rho_{\mathrm{GND}}} \tag{7}$$

where $\tau_{\mathrm{c},0}^i$ is the intrinsic 'obstacle-free' CRSS from experiments, μ is shear modulus and ρ_{SSD} and ρ_{GND} are area densities of statistically stored dislocations and GNDs, respectively. In the absence of robust experimental measurements of the precise contributions of self and latent hardening terms, models that attempt to capture them rely heavily on empirical laws, which arguably introduce unnecessary complexity and uncertainty; as such, the evolution of total statistically stored dislocation (SSD) density is controlled by a simple linear hardening rule, $\rho_{\mathrm{SSD}} = \rho_{\mathrm{SSD},0} + \gamma^{\mathrm{st}} p$, where $\rho_{\mathrm{SSD},0}$ is the initial SSD density (pre-deformation), γ^{st} is a material constant and p is total cumulative plastic strain. Calculating GND densities which arise from lattice curvature is much more involved and was previously described by Xu et al. (2021). It is assumed that both SSDs and GNDs contribute equally to hardening on all slip systems. For the model, room temperature and temperature dependent elastic constants are given in Table 3. The values presented here were previously reported and validated against macroscopic experimental stress-strain data (Liu et al., 2020). Temperature-dependent values of elastic stiffness tensor components were extracted from Fisher and Renken's work (Fisher and Renken, 1964) and were approximated as linear functions over the temperature range 293 K to 623 K.

As with elastic deformation, grain-scale plasticity in Zr alloys is highly anisotropic. Room temperature CRSS values for various slip systems which were measured experimentally by Gong et al. (2015) using micro cantilever testing, are used here (see Table 3). Subsequent high temperature modelling work by Liu et al. (2020) enabled extraction of a temperature dependent prismatic CRSS; assuming the ratio of prismatic CRSS to that of other slip systems remains constant at elevated temperatures, a simple linear approximation is needed to obtain high temperature basal and pyramidal slip strengths, as shown in Table 3. However, the exponential decay temperature for prismatic slip given in Table 3 (514.7 K) disagrees somewhat with that reported by Wang et al. (2019) for basal slip (807.7 K). Despite this discrepancy, the values reported here were previously shown (Liu et al., 2020) to yield reasonable agreement with published experimental data (Derep et al., 1980).

For the mechanistic slip rule (Eq. (5)), the various physical constants are presented in Table 4. Due to there being negligible change to the strain-rate sensitive parameters, ΔV, ΔF, at elevated temperatures (Cuniberti and Picasso, 2001), it is assumed that these values are constant in this work (in the temperature range 293 – 613 K). Similarly, in this model Burgers vector magnitudes and mobile dislocation density are assumed unaffected by temperature, since the rates of dislocation pinning, annihilation, and generation are not precisely known.

A CPFE-based modelling methodology is developed for quantitative assessment of the influence of hydrides on the cyclic accumulation of strain during thermomechanical loading Fig. 2

The finite element model, which is outlined in Fig. 3, shows that ahead of the notch a CPFE region of interest is defined containing the microstructure of sample H1 in its pre-hydrided state. Hence, in combination with experimental DIC strain measurements of the same microstructure in the hydrided state, subjecting the model to the same external environmental conditions will provide a like-for-like comparison, such that hydride strain ratcheting effects can be isolated and quantified. The beam is represented by partial extrusion

Table 4
Constants used in mechanistic slip rule, assumed temperature independent.

Property	Symbol	Value	Units
Mobile dislocation density	ρ_{m}	0.01	μm^{-2}
Escape attempt frequency	ω	1.0×10^{11}	Hz
Type ⟨a⟩ Burgers vector	$b_{\langle a \rangle}$	3.2×10^{-4}	μm
Type ⟨c + a⟩ Burgers vector	$b_{\langle c+a \rangle}$	$1.593\, b_{\langle a \rangle}$	μm
Activation energy	ΔF	0.32	eV
Activation volume	ΔV	20.93	b^3
Boltzmann constant	k_{B}	1.381×10^{-23}	JK^{-1}

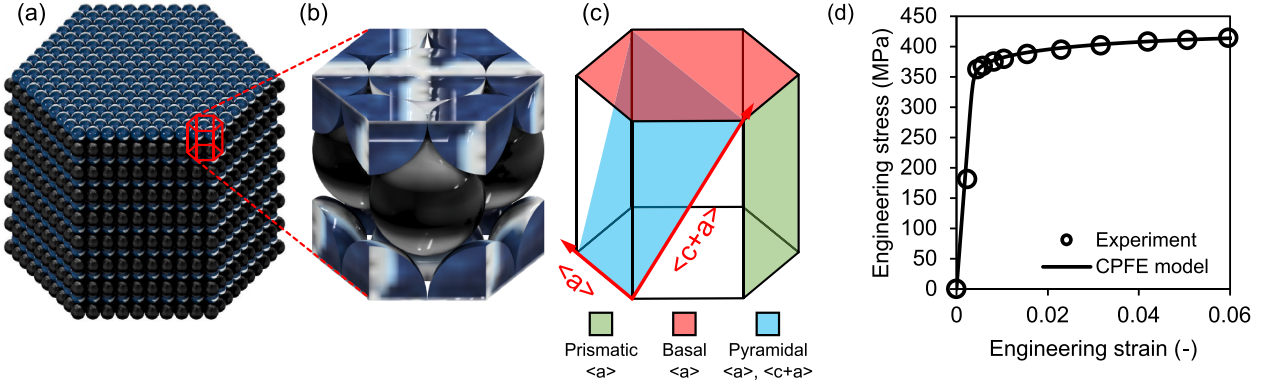

Fig. 2. HCP crystallography. (a) Schematic representation of HCP atomic structure. (b) Repeating unit cell of HCP crystal. (c) Major HCP-Zr-deformation slip systems represented within unit cell (only first order pyramidal slip is shown here). (d) Comparison of CPFE-predicted room temperature mechanical response in (hydrogen-free and unirradiated) Zircaloy-4 with published experimental data (Farrell et al., 2004). The simulated polycrystal temperature was constructed according to the experimental description; simulation details were previously reported (Long et al., 2024).

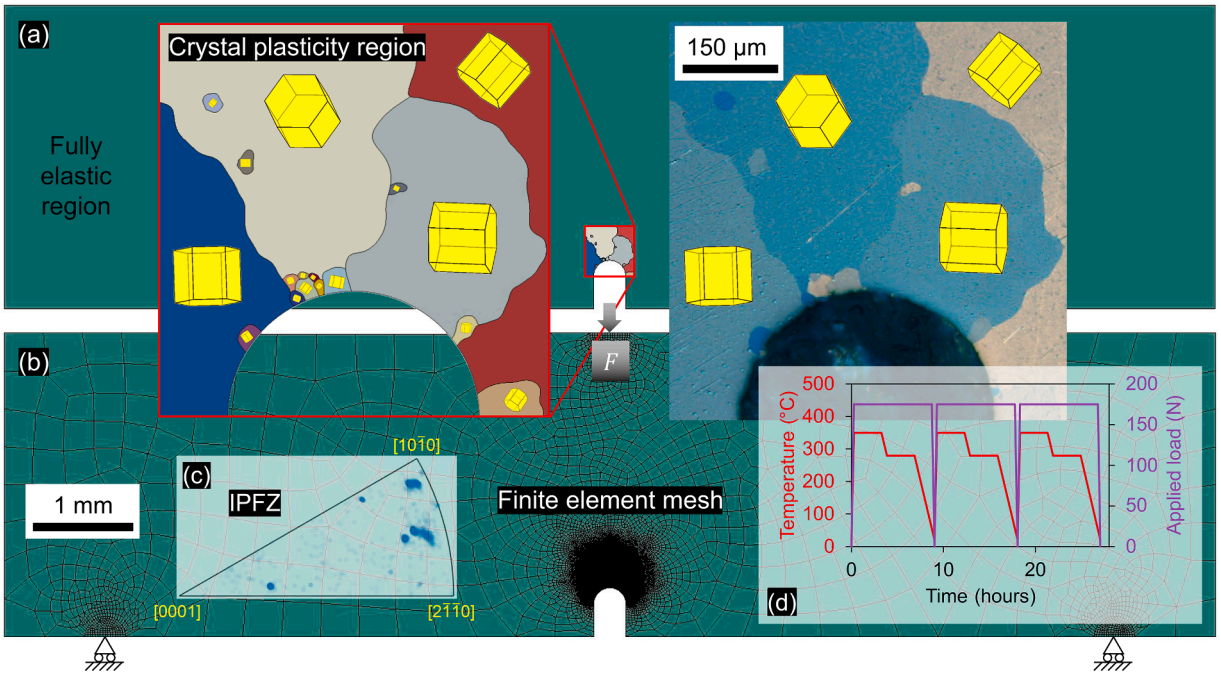

Fig. 3. CPFE modelling representation of sample H1 in its non-hydrided state for isolation and quantification of hydride ratcheting effects through comparison with experiments. (a) Full model with crystal plasticity and fully elastic regions. The crystal plasticity region is based on EBSD from sample H1 prior to hydrogen charging. A polarised light micrograph of the region of interest is also shown. (b) Mesh refinement and boundary conditions. 5 μm elements were deemed sufficiently small within the crystal plasticity region to achieve mesh convergence based on notch root stress. (c) Inverse pole figure for sample H1 in the z-direction (out of plane). (d) Three cycles of the thermomechanical loading history.

(100 μm) of its outer profile and notch microstructure. As indicated by Fig. 3(a), the region outside of the crystal plasticity region is modelled as fully elastic, with elastic properties corresponding to a crystal orientation oriented such that its c-axis is in-plane and vertical, and is chosen at random since sample H1's microstructure is not very strongly textured. Fig. 3(c) shows a set of three thermomechanical cycles, which are applied to sample H1 (experimentally and via the model). The thermomechanical cycle used here is loosely based on real pressurised water reactor operation conditions and was previously published by Liu et al. (2021). The applied load is selected to be sufficient to generate a stress of 500 MPa (at room temperature) at the notch root (Honniball et al., 2021), which is first determined using the model. The load is initially increased linearly over time, assuming a linear stress rate of 1 MPa/s, followed by a dwell period, and unloading. The temperature cycle consists of a linear upward ramp through time, followed by two successive dwell and cooling periods. The maximum temperature of 340 °C is achieved over the same period taken to reach the maximum applied load (at a heating rate of 2 °C/s), which is followed by a 3-hour dwell.

At this temperature (and bulk hydrogen content of 200 ppmw), most of the hydrogen is brought into solution. The temperature and load dwell periods allow for stress-driven hydrogen diffusion to occur. After the dwell, the first cooling stage occurs at 120 °C/hour until reaching 280 °C. Where stress-driven diffusion has occurred, the local hydrogen content in some locations, e.g., at grain boundaries, will be sufficient to precipitate hydrides, while in regions with lower hydrogen content, the hydrogen remains in solution. Based on the bulk hydrogen content, the 280 °C dwell temperature is between the temperature for terminal solid solubility for precipitation (TSSP) and terminal solid solubility for dissolution (TSSD). The second 3-hour dwell period therefore facilitates additional steady-state stress-driven diffusion (of soluble hydrogen) and hydride precipitation. Lastly, the final cooling stage of each cycle will result in the precipitation of virtually all remaining hydrogen and is likely the most dominant source for intragranular hydride precipitation. For a detailed analysis on the influence of initial microstructure on hydride precipitation, the reader is referred to the work of Liu et al. (2021). It is important to note however, that whilst the thermomechanical history is selected on the basis of industry relevance and of the hydride dissolution and precipitation curves, it may be beneficial for future studies to explore temperature ranges beyond those within the scope of the current study.

3. Results and discussion

3.1. Intragranular hydride precipitation strains

Because of the obfuscation of much of the free surface of sample H1 after thermal load (due to oxidation), DIC data is limited to regions in which the speckle pattern has remained detectable. Image contrast was increased by 20 % during post-processing to improve pattern detection. Moreover, measurements of strain have been limited to the end of each thermomechanical cycle due to difficulty in

obtaining subset pattern matches between the initial (room temperature) reference image and mid-test (high temperature) images as the intense illumination of the sample from the IR lamps floods the signal. Consequently, total (elastic + plastic) strain (assuming zero elastic strains in the unloaded state) and hence stress measurements are unattainable in the current study. This first section is focused on interesting DIC-based strain measurements around an intragranular hydride stringer taken after the first thermomechanical cycle (in the unloaded state and at room temperature). The location of the hydride is shown in the micrograph at the left of Figure 4; it is reasonably far removed from the notch tip, and hence, any measurements of residual strain are assumed to be dominated by precipitation. The hydride is assumed to have nucleated at a second phase particle, which have been shown to trap mobile hydrogen atoms (Jones et al., 2021). Prior to the first cycle, there were no hydrides in this location. Focusing firstly on the set of in-plane strain distributions at the top of Fig. 4, ε_{xx}, ε_{yy} and ε_{xy}, hydride precipitation is shown to result in strain localisation at the centre of the hydride, the outline of which is overlaid on each image. Normal strains, ε_{xx} and ε_{yy} are shown to localise towards the top and bottom of the hydride, respectively, while the shear strain distribution is reasonably uniform. The maximum strain magnitude in any direction is around 2.5 %.

However, since δ hydride precipitation has a known morphological and crystal orientation dependence, the set of strain distributions shown at the bottom of Fig. 4 correspond to the same dataset within a new frame of reference, $x' - y'$, such that the x' direction is orthogonal to the hydride stringer feature (i.e., approximately orthogonal to the prior α basal plane), and the y' direction is parallel to it. The resultant strains, $\varepsilon_{x'x'}$, $\varepsilon_{y'y'}$ and $\varepsilon_{x'y'}$ yield profoundly more interesting results, showing extreme localisation within the hydride (of up to 4 %) in the x' direction, which is maximised near either hydride end. Strikingly, the $\varepsilon_{y'y'}$ strain distribution shows virtually no correlation with the hydride location, despite the theoretical volumetric misfit strain for precipitation of 4.58 % within the prior α basal plane (note that for the current crystal orientation, the same strain is expected in the out-of-plane direction). Similarly, there is no clear correlation between the rotated shear strain field and hydride location, which is unsurprising. Carpenter's (Carpenter, 1973) theoretical volumetric misfit strain tensor for precipitation of a δ hydride platelet, i.e., with perfect stoichiometry, is given by Eq. (8).

$$\boldsymbol{\varepsilon}_{\mathrm{vm}} = \begin{bmatrix} 0.0458 & 0 & 0 \\ 0 & 0.0458 & 0 \\ 0 & 0 & 0.072 \end{bmatrix} \tag{8}$$

where the first and second normal components correspond to the ⟨a⟩ (matrix basal plane) directions and the third normal component corresponds to the HCP c-axis direction. It is important to note that this strain tensor is based on a single hydride platelet, and hence is likely to differ somewhat from the strains which manifest from the precipitation of an entire hydride stringer (consisting of a series of platelets stacked in the *deck of cards* configuration (Perovic et al., 1983)). Here it is assumed that due to the close packed nature of these hydride features, they behave as continuous media. The CPFE model is utilised to gain mechanistic insights into this DIC strain data. In the first instance, a simplistic representation of the stringer feature is generated via a line of finite element nodes on the free surface (plane stress boundary conditions) at the same location as that experimentally observed (see Fig. 5(a)). At each node, the (rotated) volumetric misfit tensor given by Eq. (8) is applied incrementally and linearly over a precipitation period, which is assumed here to coincide with the entire second cooling period of the first thermomechanical cycle. Within the user-material subroutine code, the volumetric misfit strain increment, $\Delta\boldsymbol{\varepsilon}^{\mathrm{vm}}_{t+\Delta t}$, is incorporated within the crystal plasticity trial stress (within an implicit integration

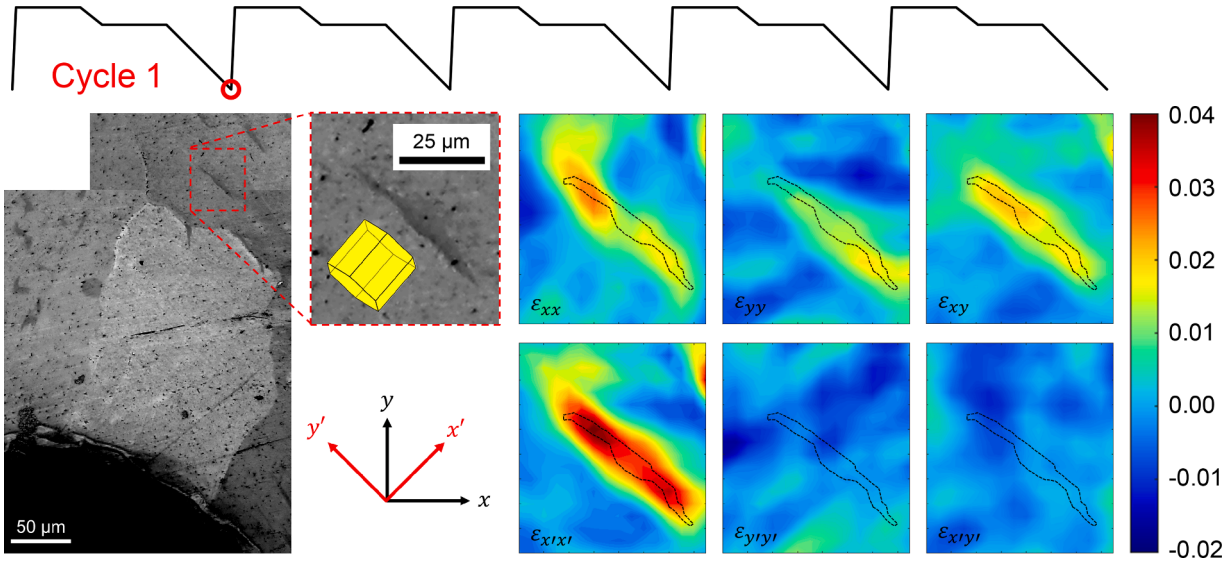

Fig. 4. Components of the DIC-measured residual strain fields around a new hydride feature in sample H1 after a single thermomechanical cycle. The 25 μm scale bar corresponds to all strain contour plots.

scheme) as an inelastic term, in the same way as the thermal strain increment, $\Delta\boldsymbol{\varepsilon}^{\mathrm{th}}_{t+\Delta t}$, as shown in Eq. (9),

$$\boldsymbol{\sigma}^{\mathrm{tr}} = \boldsymbol{D}\left(\boldsymbol{\varepsilon}^{\mathrm{e}}_{t} + \Delta\boldsymbol{\varepsilon}_{t+\Delta t} - \Delta\boldsymbol{\varepsilon}^{\mathrm{th}}_{t+\Delta t} - \Delta\boldsymbol{\varepsilon}^{\mathrm{vm}}_{t+\Delta t}\right) \tag{9}$$

where $\boldsymbol{D}$ is the global stiffness matrix, given by rotating the local stiffness matrix $\boldsymbol{C}$, $\boldsymbol{\varepsilon}^{\mathrm{e}}_{t}$ is the elastic strain at time t, and $\Delta\boldsymbol{\varepsilon}_{t+\Delta t}$ is the total strain increment after time increment Δt. Hence, the modified deformation gradient becomes $\boldsymbol{F} = \boldsymbol{F}^{\mathrm{e}}\boldsymbol{F}^{\mathrm{p}}\boldsymbol{F}^{\mathrm{th}}\boldsymbol{F}^{\mathrm{vm}}$, where $\boldsymbol{F}^{\mathrm{vm}}$ is the volumetric misfit deformation gradient. The predicted strain distributions, within the conventional and rotated frames of reference, are shown in Fig. 5 (b). Due to morphological simplicity and absence of hydride mechanical properties in the model, the experimental strain distributions are not captured precisely. However, the model does capture the most important effect, which is maximised strain localisation in the x' direction.

Moreover, the model predicts an initially counterintuitive y' strain distribution, which is compressive throughout the hydride region, with compensatory tensile hot spots at either end. In this simplistic analysis, the key difference between strains in the x' and y' directions is that volumetric expansion in the x' is only (primarily) inhibited by the surrounding grain's resistance to deformation, while expansion in the y' direction is opposed by the simultaneous expansion of other 'points' along the hydride. Hence, the extreme case of y' expansion along the representative hydride line is counter effective and leads to compression (in this case) for purely morphological reasons. Hence, it can be deduced that for the less extreme example of an actual hydride stringer, its morphology leads to the inhibition of volumetric expansion within the prior α basal plane, with maximum straining along the HCP c-axis direction.

To study this effect in greater detail, the model is modified to account for the hydride's actual (2D) morphology and size. Fig. 6 (a) shows this enhanced hydride representation, which is based on an optical micrograph of the hydride taken after the first thermo-mechanical cycle. In this unique and preliminary case study, the hydride is represented using only its anisotropic elastic properties, i.e., plastic deformation is unaccounted for during precipitation. Hence, prior to the hydride precipitation event, the region of material which is to be occupied by the hydride is initially prescribed the matrix orientation elastic properties (and is fully elastic). Based on post-test EBSD analysis, the measured hydride orientation (which satisfies the δ hydride orientation relationship) is utilised to calculate the resultant global compliance matrix, i.e., after precipitation. Hence, in parallel with the incremental application of the volumetric misfit strain over the entire hydride region, the compliance matrix is also set to evolve by linear interpolation between the temperature-sensitive Zircaloy-4 compliance matrix (no precipitation) and the room temperature hydride compliance matrix in the correct orientation, corresponding to full precipitation. Properties for the δ hydride compliance matrix are obtained from Olsson et al. (2014).

The strain field results from this model are presented in Fig. 6 (b). Firstly, the results within the original $x-y$ reference frame show slightly under-predicted normal strains, while oddly capturing increased localisation of each component (x and y) at the bottom and top of the hydride, respectively, as opposed to the experimentally observed localisation at the respective top and bottom. The shear (xy) component of strain is mostly localised near the hydride-matrix interface and at the ends of the hydride. In each case, substantial compressive strain localisation is predicted within the matrix, near the hydride-matrix interface. As shown by the rotated strain distributions, the interfacial matrix compressive strains are primarily along the x' direction. The x' strain distribution also shows that this is a countereffect of substantial tensile strain localisation within the hydride, near the interface. While the experimental x' strain distribution is not precisely captured by the model (which is likely due to not incorporating plasticity within the hydride), the important trends are captured, which include: (i) maximum strain localisation within the hydride in the x' direction, (ii) increased x' strain localisation near the hydride ends, (iii) virtually no discernible linkage between the y' and $x'y'$ strain distributions and the hydride itself, and (iv) asymmetric localisation of strain at opposing ends of the hydride in the x and y directions, respectively. The Von

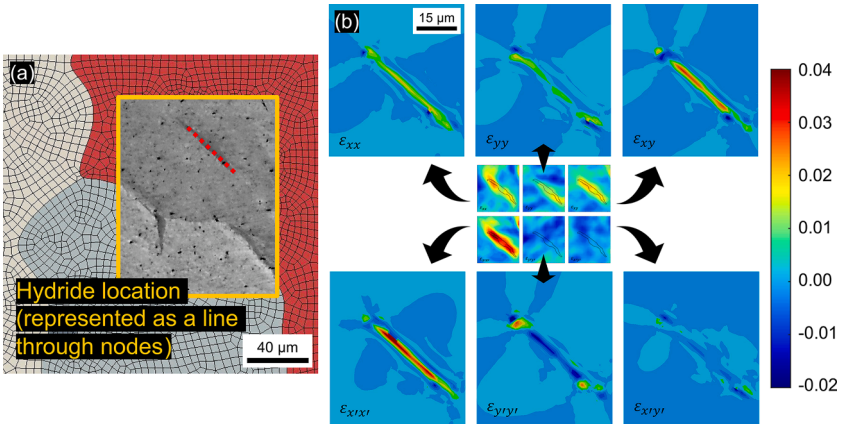

Fig. 5. (a) Simple line-of-nodes representation of hydride of interest to understand the link between the combined hydride morphological and crystallographic (in terms of volumetric misfit only) orientation and the resultant precipitation strain fields. (b) Resultant strain distributions after single cycle precipitation. The volumetric misfit strain tensor is applied to each node in parallel, with strain increasing linearly over time from 0 at the beginning of the second cooling stage, and maximum at the end of the cycle. An extract of the experimental strain fields are shown in the centre for comparison.

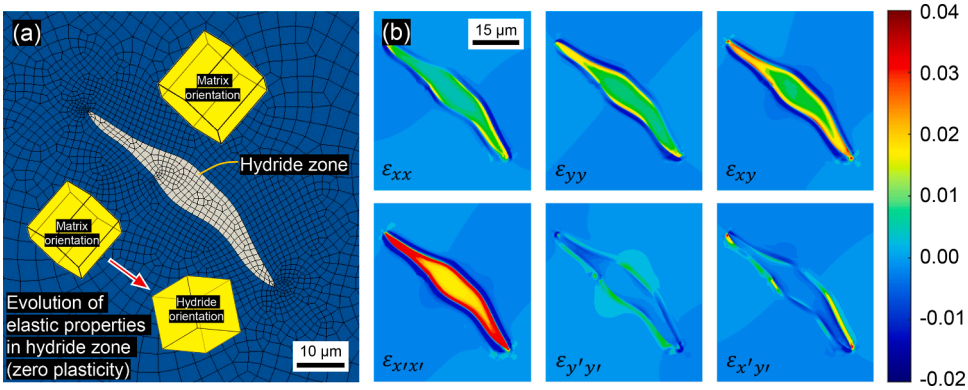

Fig. 6. (a) Modified 3D finite element representation of hydride of interest, incorporating elastic properties which evolve linearly between those of the matrix orientation and of the hydride orientation, assuming the same precipitation period as above. (b) Resultant distributions of strain, with linear elastic hydride properties, and full matrix elastic-plastic deformation.

Mises stress distribution near the hydride tip, presented in Fig. 7, can explain the discrepancies between experimental strain measurements and predicted strains based on a fully elastic hydride model.

Due to volumetric expansion throughout the hydride, which is inelastic, the response of the surrounding matrix is to impose a compressive stress on the hydride (Khan et al., 2021). Due to its purely elastic response in the current model, there is no stress relaxation within the hydride, resulting in extreme localisation of plastic strain within the surrounding matrix, and GPa-level compressive stresses within the hydride; hydride stresses have been omitted from Fig. 7 for this reason. Based on the uniform application of volumetric misfit (tensile) strain throughout the hydride, localisation of x' direction strain within the hydride, near the hydride-matrix interface, is reflected by an increased compressive elastic strain (and stress) towards the centre of the hydride, due to localised stress-relaxation afforded by the matrix. Hence, with the incorporation of crystal-level hydride plasticity, this new modelling approach could potentially accurately capture the experimental DIC measurements and provide highly valuable insights into damage localisation during single and multi-cycle hydride precipitation. The hydride tip tensile hydrostatic stresses suggest that hydrogen redistribution and precipitation are likely to occur locally as a result of the initial precipitation, which agrees with similar modelling work (Taherijam et al., 2023). Whilst the aim of modelling the hydride precipitate stresses was not the purpose of this sub-study, this is an important result in its own right, as it indicates strongly that hydride plasticity is an important feature of the precipitation process.

3.2. *Hydride strain ratcheting*

In this section, the issue of hydride strain ratcheting (the cyclic accumulation of strain due to the dissolution and reprecipitation of hydrides) is investigated via cyclic thermomechanical loading of sample H1. DIC data showing the cyclic accumulation of strain within sample H1 is compared quantitatively with CPFE-based predictions in the absence of hydrides. Fig. 8 shows electron micrographs of a local region of interest ahead of the notch tip, consisting of several grain boundary hydride features after three thermomechanical cycles. The measurement path used to compare DIC and CPFE-based strains through the same region is also shown (see Fig. 9).

Path-based line plots of the residual strain distributions (with strain measured in the path direction) across this region of interest for the first three thermomechanical cycles are shown in red (with increasing transparency) in Fig. 9 (a), with the corresponding measurement path shown above. Vertical red lines indicate the points of intersection between the measurement path and the three hydride locations shown in Fig. 8. Fig. 9 (a) also shows the equivalent non-hydrided CPFE-based strain distributions through the same region

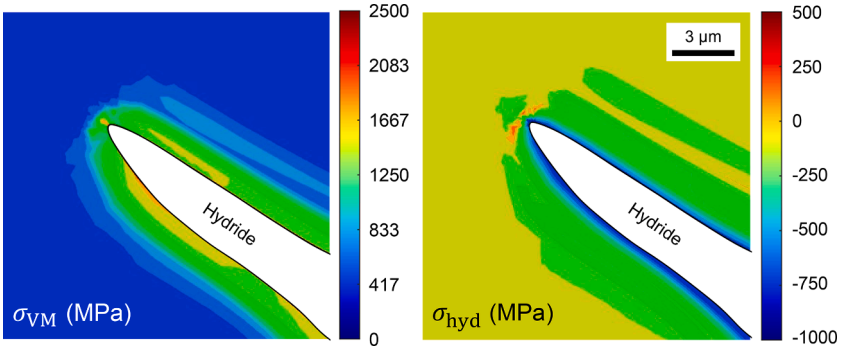

Fig. 7. Von Mises (σ_{VM}) and hydrostatic (σ_{hyd}) stress distributions at hydride tip after precipitation. Distributions of stress within the hydride have been omitted. The scale bar in (b) applies to (a) and (b).

using black lines (with increased line transparency for increasing number of cycles). The measurement path is shown in the context of the CPFE-predicted residual strain distribution in Fig. 9 (b), which also shows the underlying microstructure in this region in greater detail. From left to right along the measurement path, a very large grain is traversed before encountering strain localisation at the first grain boundary, followed by several much smaller grains, within which, very little strain localisation is predicted, followed by crossing a slightly larger grain in which significant localisation is predicted, particularly near boundaries at either side, which is then followed by crossing the last grain boundary into another large grain.

For the hydrided case, Fig. 9 (a) shows that in regions where hydrides have been observed, residual strain is maximised (locally), and is shown to increase cyclically in the same locations, particularly in the left-hand most location, where the x-direction strain reaches up to 6 % after the third cycle. Interestingly, the peaks at each of these three locations are rather close to strain peaks predicted by the non-hydrided CPFE model. A key difference, however, is that in the hydrided case, strain is maximised at the matrix boundaries (where hydride precipitation has occurred), while in the non-hydrided case, strain is maximised near the boundaries, within the softer grains, due to strain gradient (GND) hardening near the boundaries. Under the applied load (during the dwell period), most of the measurement path region is in tension, with tensile hydrostatic stress hot spots at grain boundaries, within 'hard' grains (hard referring to a grain with a greater c-axis component in the horizontal loading direction than its neighbouring grain). Since tensile hydrostatic stresses are known to promote hydrogen ingress, it follows that hydride precipitation would occur along each of the three grain boundaries which are shown to promote the greatest levels of strain localisation. Another key difference between experimental and CPFE-predicted strain distributions are the substantial residual compressive strains which develop adjacent to regions showing highly localised tensile strains. This is a direct consequence of the volumetric expansion during precipitation, as compressive strains develop in the matrix to accommodate these changes. Hence, no such compressive residual strains are predicted by the CPFE model. This observation is consistent with the modelling results (for intragranular hydride precipitation) discussed earlier. Lastly, the experimental measurements of the cyclic accumulation of strain within tensile and compressive hot spots is not predicted by the CPFE model; only marginal strain accumulation is predicted. Hence, this helps to confirm that the strains accumulating within the hydrided sample are as a direct consequence of hydride dissolution and re-precipitation during each thermomechanical cycle. This is therefore the first known measurement of hydride strain ratcheting at the microstructural level.

The cyclic accumulation of x' direction strain and GNDs around the intragranular hydride from Fig. 4 has also been measured and is presented in Fig. 10 and (quantitatively) in Fig. 11 for five thermomechanical cycles. Here, the GND density distributions are based entirely on gradients of plastic strain measured using DIC (as described earlier) and therefore, do not distinguish between volumetric expansion strains within the hydride and plastic strains within the hydride. Hence, measurements of GND density should only be considered from outside the hydride. In Fig. 10, the outline of the initial intragranular hydride is shown for the first cycle, and in the fifth cycle, the final hydride is shown along with several smaller intragranular hydrides surrounding it. From Fig. 10, a very clear cyclic strain ratcheting effect is shown. Initially, there is a band of tensile strain (linked with volumetric expansion) within the hydride, which is shown to increase cyclically, in parallel with the development of bands of compressive strain at either side of the hydride (which was previously predicted for a single cycle using the CPFE model). Using a horizontal measurement path crossing the centre of the hydride, Fig. 11 (a) shows that the initial strain distribution is entirely tensile, with a maximum strain of around 4 % at the centre of the hydride. This value is shown to increase by more than a factor of two after five cycles, at which point the strain ratcheting effects appear to saturate. The bands of compressive strain are shown to reach almost −6 % within the surrounding matrix.

For the first cycle, the distribution of GNDs is shown to surround the hydride, with maximum densities of up to 100 μm^{-2} (see Fig. 10

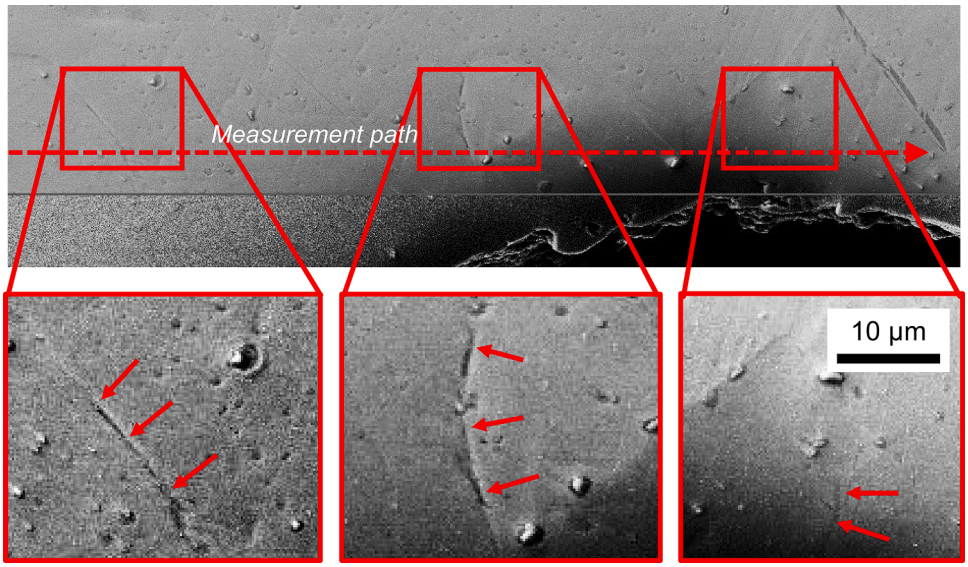

Fig. 8. Electron micrographs showing grain boundary hydride precipitation at the notch after three thermomechanical cycles.

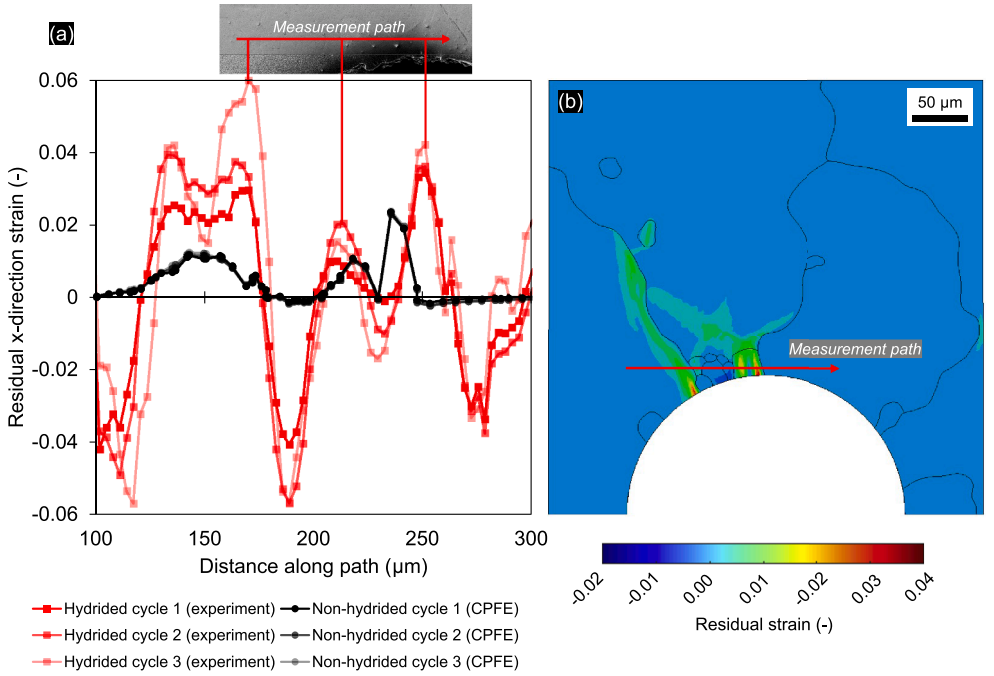

Fig. 9. (a) Cyclic evolution of residual *x*-direction (horizontal) strain distribution along a path for three thermomechanical cycles, corresponding to the region of interest outlined by Fig. 8 experimentally and from the CPFE model, which does not account for hydride precipitation effects. (b) Measurement path and resultant CPFE-predicted *x*-direction strain field after three cycles.

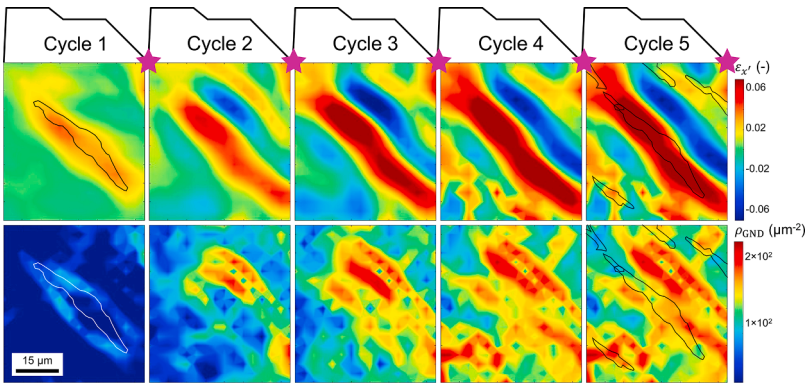

Fig. 10. Cyclic evolution of the x' strain and GND density fields around the hydride of interest for five thermomechanical cycles. Data has been recorded at the end of each cycle, as shown using purple stars.

and Fig. 11 (b)). Subsequently however, the development of bands of compressive strain around the hydride is shown to generate strain gradients which make the GND distribution somewhat more perplexing. Nevertheless, the GND density is also shown to increase and (almost) achieve saturation after five thermomechanical cycles, with maximum values of around 200 μm^{-2}. These levels are comparable with values predicted ahead of crack tips (Long et al., 2022), demonstrating the potentially highly damaging effects of hydride precipitation and ratcheting.

After the fifth cycle, the newly formed hydrides (which are overlaid in Fig. 10) are potentially linked with the development of the GND network around the original hydride, though there is no clear linkage between their locations and that of the GNDs. For future work, further CPFE model development, accounting for the development of plastic strains within the hydride, will be required to fully appreciate the new experimental data presented in this section. The modelling work presented here was primarily included to complement the experimental results. Specifically, the simple elastic model has proven very useful in understanding the interesting hydride strain directionality. Moreover, we show using a hydride-free analysis that hydride precipitation locations correlate strongly with localised plastic deformation. It is envisaged that these results will lead to future development of holistic models for hydride-induced deformation.

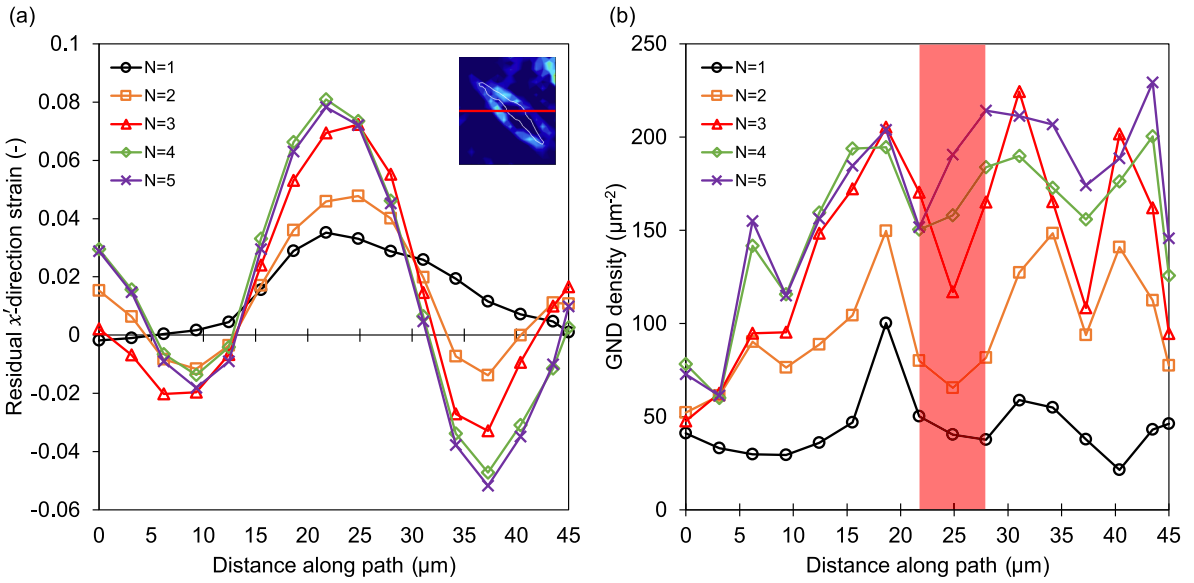

Fig. 11. Path-based distributions of (a) x' strain and (b) GND density over five thermomechanical cycles (hydride location marked in red). The path position is shown relative to the hydride in red in (a).

3.3. Isothermal fatigue crack propagation

In this section, the results of isothermal (room temperature) FCG testing are presented; as discussed in Appendix A, the thermal gradient heat treatment is not necessary here. Fig. 12 (a) is a polarised light micrograph showing the microstructure (sample H2) used in the first FCG study. Number annotations, 1 – 3, point to intergranular, twin, and intragranular hydride features, respectively. Cyclic $R = 0$ loading is applied here, with loading frequency 0.1 Hz, ensuring sufficient time to capture images for DIC. Fig. 12 (b) shows the resultant crack path through sample H2 during testing (an image from the long-range optical microscope) after several hundred fatigue cycles. The primary Zircaloy-4 grain and hydride boundaries are overlaid with black and yellow lines, respectively.

The crack path shown in Fig. 12 (b) is unlike any published crack path in non-hydrided zirconium alloys in that it has two main sections: (i) that which nucleated at the notch and propagated through the microstructure (in the usual manner) and (ii) the double-ended crack which nucleated near-instantaneously (within the first 5 fatigue cycles) along a grain boundary hydride feature at region D, despite it being reasonably far removed from the notch. Throughout the test, cracks (i) and (ii) propagate independently of one another, before eventually linking together, leading to detrimental sample failure. Surprisingly, the crack which nucleated at the notch did so within the middle of a grain which is bounded by hydrides at either end – there may be substructural reasons for this, particularly since grains at notches and other surfaces are often much smaller than those within sample centres. The seemingly random nucleation of a crack at region D highlights the undesirable effect of uncertainty in structural integrity due to the presence of brittle hydride features. Fig. 13, Fig. 14, and Fig. 15 present post-deformation electron micrographs of subregions A to E (see Fig. 12), highlighting the various fatigue (and static) crack propagation mechanisms in Zircaloy-4. Fig. 13 shows details of crack (i) within the first grain before (region A) and after (region B) a change in crack direction.

The electron micrograph of region A in Fig. 13 shows multiple parallel sub-micron prismatic plane cracks (which are also parallel with the primary crack growth direction this region). The shortest crack sections are observed to nucleate between hydride platelets (darker, near-horizontal features), which indicates that the nano to sub-micron hydride platelets are responsible for driving prismatic slip localisation and hence, the nucleation of crystallographic facets. There are also examples of these facets extending through and beyond the brittle hydride platelets, which is likely to affect FCG rate. Moreover, region B, shown in Fig. 13, highlights that after a change of crack direction, the crack path remains dominated by crystallography, i.e., slip plane orientation, as indicated by blue arrows, and pyramidal slip plane shown. The short crack segments corresponding to green arrows however appear non-crystallographic. Nevertheless, it is important to note that observations of intragranular FCG along prismatic and pyramidal planes within a grain of this orientation are consistent with those within non-hydrided Zircaloy-4 counterparts (despite interactions with intragranular hydrides, which are shown here).

Region C is microstructurally complex. It consists of several interconnected sections of grain boundary and triple junction hydrides around multiple matrix grains. The snapshot to the left of Fig. 14 shows that once the intragranular notch crack (regions A and B) reaches region C, the crack path becomes dominated by grain boundaries, which is entirely atypical for non-hydrided zirconium alloys (Wan and Dunne, 2020; Zeng et al., 2022). This is however consistent with Garlea *et al.*'s observations (Garlea et al., 2010). It is shown to first propagate vertically along a grain boundary hydride between two triple junctions, before veering rightward along subsequent grain boundary hydrides; an increased magnification micrograph of one such region is shown in the right-hand side of Fig. 14.

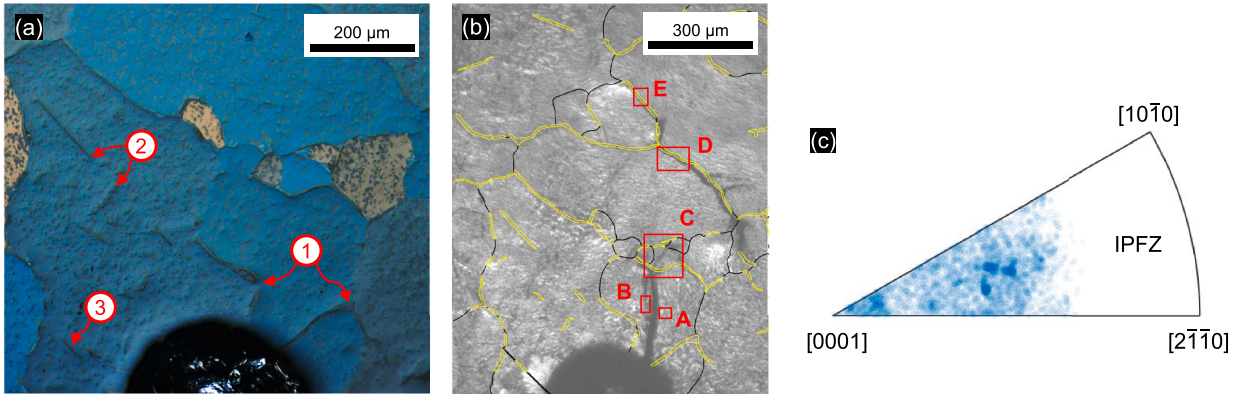

Fig. 12. (a) Microstructure H2 with various hydride features: (1) grain boundary (intergranular) hydrides, (2) intragranular hydrides, and (3) twin boundary hydrides. (b) Snapshot from DIC microscope of sample H2 after several hundred $R = 0$ fatigue cycles and substantial crack propagation; a fatigue crack is shown to emanate from the notch, while a separate grain boundary hydride driven crack is also shown to have propagated. Regular grain and twin boundaries are shown using black lines, while yellow lines indicate hydride-matrix boundaries (most hydrides shown here are large grain boundary hydrides). Regions A – E will be shown subsequently in greater detail. (c) Inverse pole figure for sample H2 in the z-direction (out of plane).

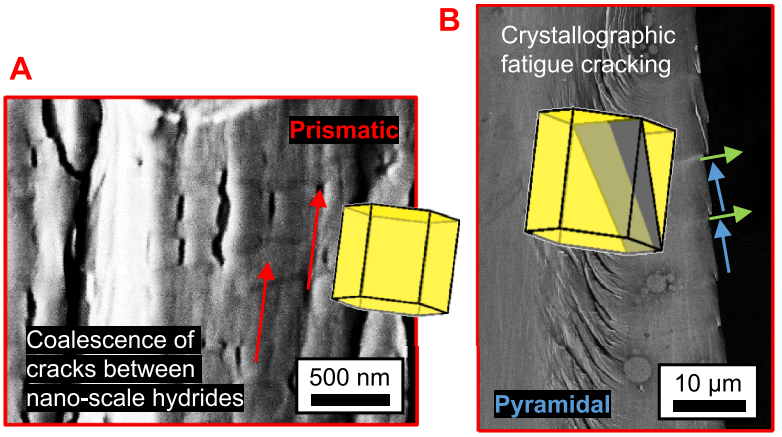

Fig. 13. Regions A and B from sample H2. Region A is adjacent to the primary crack and shows multiple prismatic microcracks which are parallel to the primary crack growth direction. Cracks are shown to form between horizontal (matrix basal) hydride platelets and appear to coalesce. Region B is within the same grain, after a slight crack path direction change (which also appears crystallographic).

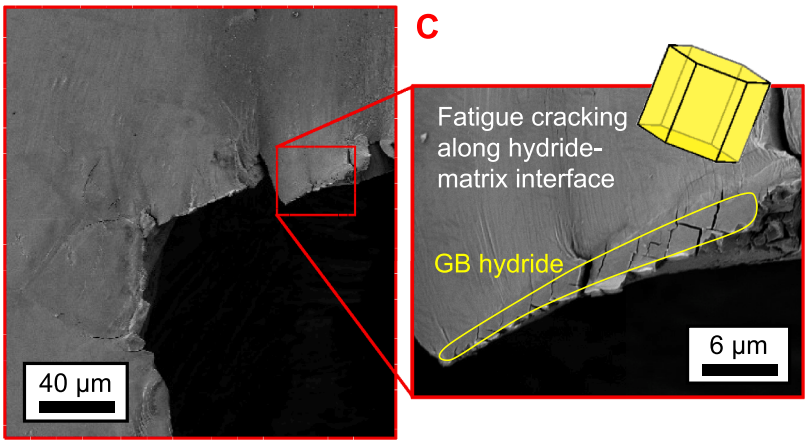

Fig. 14. Region C from microstructure H2. A magnified view shows that the crack has propagated along grain boundary hydrides. Parallel microcracks are visible throughout the grain boundary hydride shown.

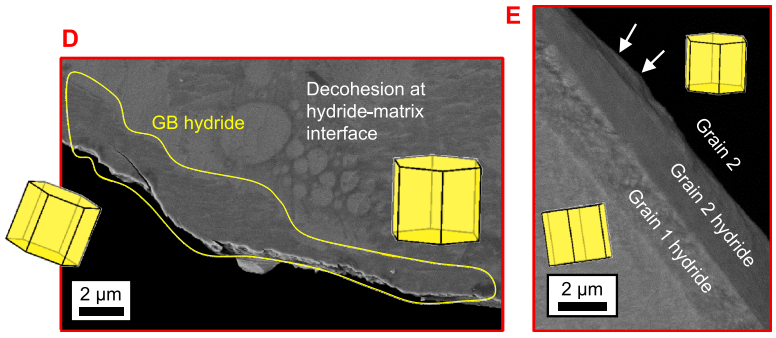

Fig. 15. Regions D and E from microstructure H2. Both regions are far removed from the primary notch crack and show examples of grain boundary hydride cracking which are apparently interfacial. In region E, due to differences in contrast, it appears that there are two different hydride orientations present, corresponding to different matrix orientations.

Here, the primary crack path is shown to have propagated non-uniformly to one side of the grain boundary hydride (which is outlined in yellow). The various parallel, cleavage-like sub-cracks throughout the grain boundary hydride appear to have strong interactions with the primary crack and indicate that the overall crack propagation direction is heavily influenced by this sub-cracking. The crack propagation mechanism, therefore, is highly complex (as compared with intragranular crystallographic fatigue cracking or matrix-hydride decohesion).

Furthermore, however, evidence of hydride-matrix decohesion can be found in sample H2, examples of which are shown in Fig. 15. As discussed previously, region D corresponds to a location for premature cracking (within the first 5 cycles). Post-deformation examination of the crack path in Fig. 15 (region D) indicates that interface decohesion is likely to have had a role in this. However, due to non-availability of the opposing crack face (due to severe deformation), it is not clear whether hydride-hydride interfaces or hydride-matrix interfaces are implicated.

It is reasonable to assume hydride-hydride interfaces are implicatedsince (i) different grain orientations result in different hydride variant orientations which exhibit detectable differences in contrast using electron microscopy, i.e., since only one matrix hydride type is distinguishable in Fig. 15, it is likely that the neighbouring grain's hydride remains attached to it, and (ii) the somewhat jagged crack face in region D may be indicative of tortuous decohesion between up to four hydride twin variants (Wang et al., 2019) at the original matrix boundary. A more distinct example of decohesion is shown at region E (see Fig. 15). Region E corresponds to an upper section of the crack emanating from region D and is along a grain boundary hydride feature. Here, it is easy to distinguish between the original grain (Grain 1), and the hydride variants corresponding to Grains 1 and 2, as annotated. Unlike the crack path in region D, this is a clear case of decohesion along the interface of Grain 2 and its corresponding boundary hydride in region E, producing a comparably uniform crack surface. Examination of Grain 2′s crack surface revealed no boundary hydride presence.

Having first discussed the various cracking mechanisms in sample H2, it is now appropriate to study FCG rates. Fig. 16 shows how the rate of crack growth (for the notch crack only) evolves with increasing crack length. Above the graph, the corresponding 350 μm region of microstructure is presented with primary crack path(s) overlaid in purple. As before, matrix-matrix and hydride-matrix boundaries are also overlaid using black and yellow lines, respectively. Vertical red lines correspond to points at which sudden changes in crack propagation rate and important microstructure interactions occur.

Fig. 16 highlights the substantial crack growth rate variability through sample H2. Initially, ahead of the notch, there is a rapid growth rate fluctuation (rise and fall between 425 and 500 μm). As the growth rate reaches a minimum at a crack length of 500 μm, the red line shows that this point corresponds to the end of at least two dramatic changes in crack propagation direction. Previous work in non-hydrided Ziraloy-4 showed that sudden changes in crack propagation direction can lead to substantial FCG rate reductions, which could therefore help to explain this sudden fluctuation. The various in-plane DIC-based strain fields are shown at this stage of crack growth (Location 1) at the left of Fig. 17. Beyond this point (within the zone corresponding to region A from before), the rate of FCG increases sharply (from 0.2 to 0.75 μm/cycle), and then continues to increase steadily to a local maximum value of around 1.5 μm/cycle at Location 2. The sudden initial increase in growth rate could be attributed to a restoration to a level commensurate with the applied SIF following the period of tortuosity. Given the relatively straight crack path and lack of microstructural obstacles in the region thereafter, it is unsurprising that the FCG rate continues to rise. Moreover, the steep rate at which FCG rate rises could be

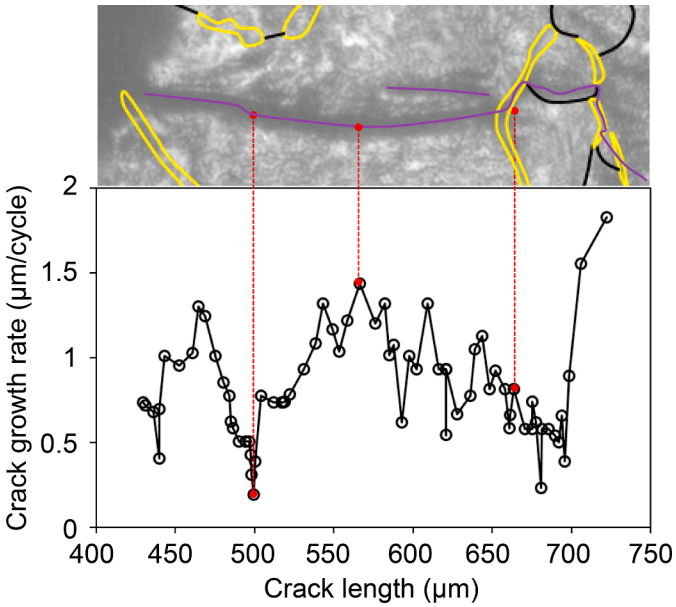

Fig. 16. FCG rate versus projected crack length of primary (notch) crack in sample H2. The primary crack path is shown above and is highlighted using a purple line. Vertical red lines correspond to important points of crack growth including sudden changes in FCG rate, changes in crack growth direction, and interactions with microstructural features.

attributed to (i) coalescence of a series of hydride platelet fractures driven by enhanced prismatic slip localisation, and (ii) an increasing level of interaction with the separately growing upper grain boundary hydride crack, i.e. crack which nucleated at region D. Evidence for (ii) is contained within the central set of DIC strain maps (particularly for ε_{xx}) in Fig. 17.

Between Locations 2 and 3 (referring to Fig. 17) of crack growth, there is a steady FCG rate decline, with several minor undulations between. While it was previously shown that between regions A and B, there is some shift in the overall crack propagation direction, this is not sufficient to explain this progressive FCG rate decline. However, the crack path outlined in Fig. 16 shows that between Locations 2 and 3, there is the seemingly random formation of an additional crack, which propagates almost parallel-wise with the primary crack. It is assumed that this crack originates from the facet coalescence mechanism discussed earlier, i.e., the localisation of strain at hydride platelet interfaces gives rise to the nucleation of new cracks. Hence, the reduction in FCG rate can at least partly be explained by the dispersion/dissipation of the primary crack tip driving force due to the formation of these new cracks. More detailed studies in which precise intragranular FCG rates are attainable, e.g., using in-situ testing in a scanning electron microscope (SEM), will be required to test this hypothesis, however. Moreover, beyond Location 3, as the crack propagates through region C (along grain boundaries etc.) the FCG rate declines even further (to a value commensurate with a crack length which is 200 μm shorter). Following from the proposed energy dissipation mechanism, it is assumed that the observed substantial crack branch formation associated with grain boundary hydride cracking (within region C) is also responsible for strain energy dissipation, and hence FCG rate reduction. The maximum shear strain plots shown in Fig. 18 reinforces this theory. Specifically, when FCG rate is maximised (Fig. 18 (b)), there is a direct and strong interaction between the upper and lower crack tips, whereas when the notch crack propagates into region C (Fig. 18 (c)), the strain field is far more diffuse and effectively orthogonal to the primary crack growth direction. An electron micrograph of region C is also presented in Fig. 18 (c) which shows significant crack branching ahead of the crack tip at this point. Upon traversing region C, crack growth accelerates enormously due to its proximity to the hydride boundary crack; beyond this, the sample failed completely.

Lastly, the FCG rate data from sample H2 is compared with published experimental data from a non-hydrided Zircaloy-4 sample with similar underlying texture (Wan and Dunne, 2020) in Fig. 19. SIF range is used here for comparison to account for differences in applied load and sample geometry, etc. Note that even in the non-hydrided case, significant crack propagation rate fluctuations were reported due to interactions with microstructure, which would require detailed micromechanical modelling for full interpretation (Long et al., 2022). Hence, with the added complexity of hydride precipitation at length scales much lower than the grain scale, further high-resolution studies will be required for comprehensive understanding. For detailed studies on the influence of underlying microstructure on short FCG rate and path, the reader should refer to our previous work (Long et al., 2022; Long and Dunne, 2023). While the SIF range applied to sample H2 is mostly higher than that of its non-hydrided counterpart, there is some overlap in the range 17 – 21 MPa$\sqrt{\text{m}}$. The data show that on average, FCG rates are twice as high in the hydrided case, despite also showing the greatest degree of rate variability, for reasons outlined earlier. At one point, FCG rate in the hydrided sample drops to a point which is twice as low as that of the non-hydrided case (corresponding to Location 1 from before) due to changes in crack direction. At around 22 MPa$\sqrt{\text{m}}$, the hydrided case FCG rate is also reduced significantly due to energy dissipation linked with additional crack nucleation and crack branching at grain boundary hydrides. In general, it is observed that intragranular and intergranular hydrides contribute to the respective acceleration and deceleration of FCG rates.

It is entirely conceivable therefore that in as-received microstructures (consisting of grains of around 10 μm diameter), hydrides may provide the beneficial effect of an overall FCG rate reduction due to increased grain boundary hydride precipitation (Birch et al., 2019; Weekes et al., 2016). While intriguing, this finding remains very much hypothesis-based, as with large-grain experiments such as

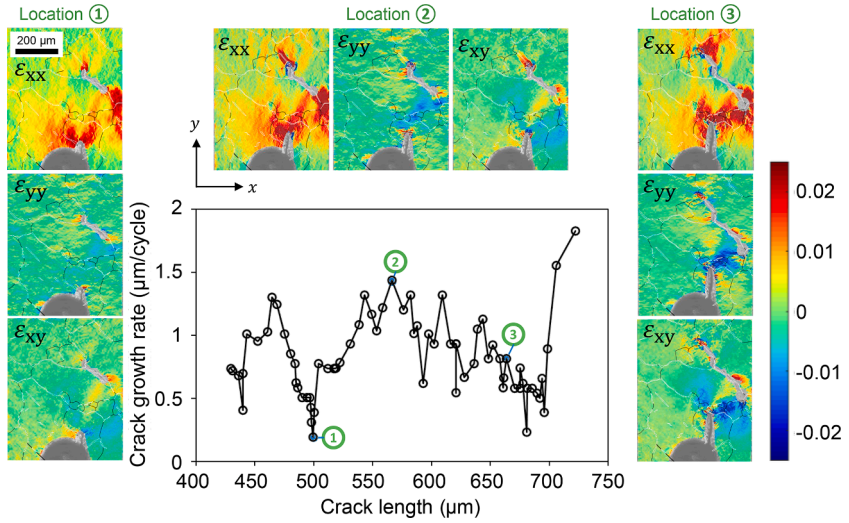

Fig. 17. DIC total strain maps at key Locations (1, 2, 3) of FCG. All maps shown correspond to the peak load of a given fatigue cycle. Normal and shear strain plots are shown.

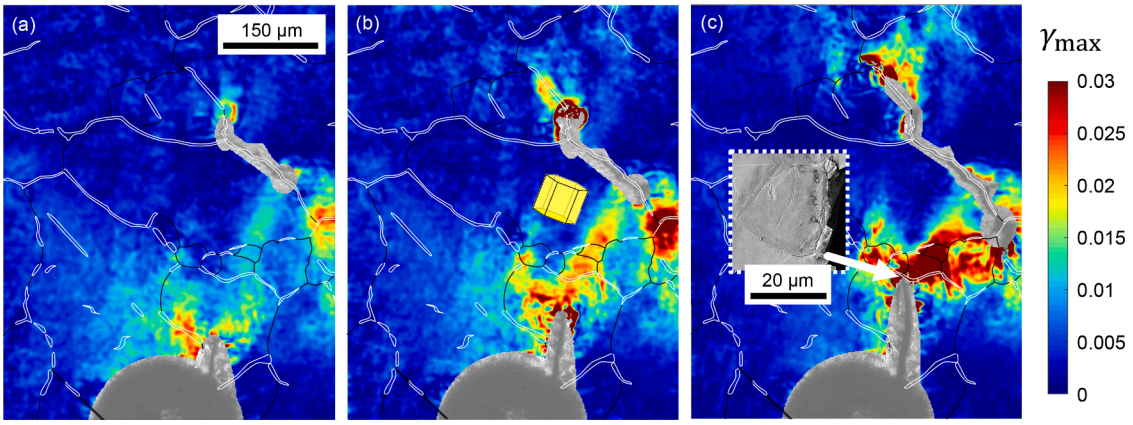

Fig. 18. DIC maximum shear strain plots at Locations ((a) 1, (b) 2, (c) 3) of FCG. Subfigure (c) shows an SEM image of the region of microstructure ahead of the crack tip, post-deformation showing crack branching throughout grain boundary hydrides.

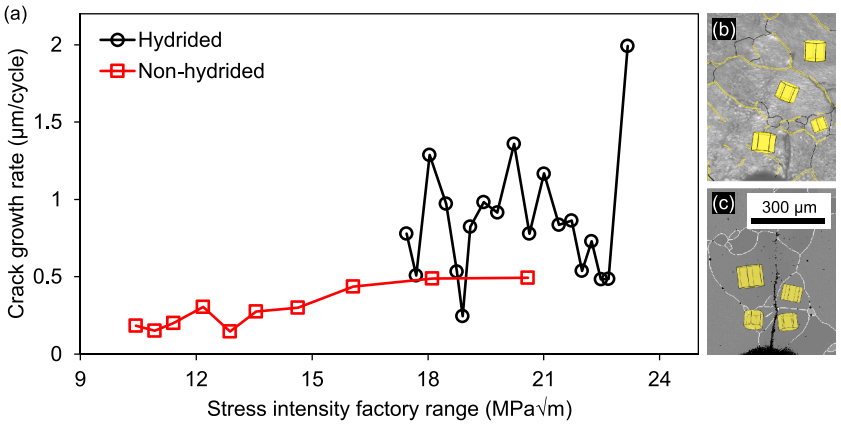

Fig. 19. Comparison of FCG rates in hydrided (sample H2) and non-hydrided (Wan and Dunne, 2020) Zircaloy-4 samples via SIF range (crack length is arbitrary when considering differences in applied load and geometry). For the non-hydrided case, the 4-point moving average of the raw data is used for clarity. (b) Sample H2 microstructure. (c) Non-hydrided sample microstructure (Wan and Dunne, 2020). The scale bar in (c) applies to (b) and (c).

this, crack-GB hydride interactions at the free surface are relatively infrequent. It is therefore anticipated that higher resolution studies will follow this work to investigate this matter in greater detail.

To gather supplementary short FCG data across lower SIF ranges (beginning at 10 MPa$\sqrt{\text{m}}$), a repeat experiment is carried out using sample H3, which is shown in Fig. 20 (a). An interesting difference between samples H3 and H2 is the notably increased proportion of twin features (formed during heat treatment) in sample H3 and hydride precipitation therein. After approximately 890 fatigue cycles with an applied notch (crack) tip SIF range of 10 MPa$\sqrt{\text{m}}$, the sudden nucleation and extension of near-mm length cracks through several of these hydrided twin features is observed, as shown in Fig. 20 (b). First, the leftward extension of the left-hand crack through the first hydrided twin from near the notch led directly to another such feature in a neighbouring grain through which it continued to propagate (until reaching the end of the twin), all within a single cycle. After 23 subsequent fatigue cycles, a virtually symmetric event occurred through an additional set of hydrided twin features. The red boxes labelled 1 – 5 in Fig. 20 (b), which track the crack paths, are shown in greater detail in optical micrographs presented in subfigures (c) to (g).

Fig. 20 (c) shows the nucleation site (region 1) of the first (left-hand) crack. The crack nucleated and propagated within and through a grain boundary hydride near the notch root before reaching the twin, at which point it is assumed to have advanced irreparably though the entire feature. The initial grain boundary hydride crack is consistent with published observations of fatigue cracking in zirconium hydrides (Li et al., 2022). The right-hand crack nucleated within the hydrided twin at the notch. However, it is interesting to note that this occurred after the left-hand crack had propagated, which is likely to have had a substantial effect on the stress state. Hence, the evidence suggests that while hydride twin features are detrimental to structural integrity, they appear to require external stress concentration features (i.e., cracks nucleating in a more conventional manner) before manifesting themselves as such. Fig. 20 (d) reveals that at location 2, an interconnecting hydrided twin feature was also fractured, though not to the same extent, as it terminated shortly thereafter. Similarly, Fig. 20 (e) shows the sharp crack path transition between one hydrided twin feature and

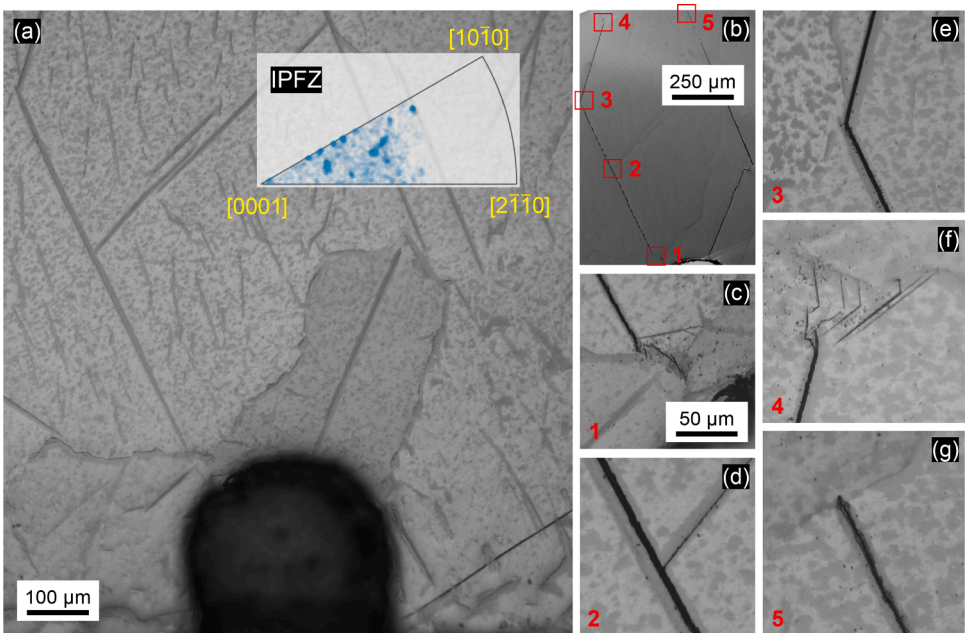

Fig. 20. (a) Sample H3 microstructure prior to room temperature fatigue testing and (b) after approximately 890 fatigue cycles, showing mm-scale cracks which suddenly traversed the sample along twin hydrides. Subfigures (c) to (g) are increased magnification images of the cracks, corresponding to regions 1 – 5. The scale bar in (c) also applies to subfigures (d) to (g). The inverse pole figure shown in (a) corresponds to the z-direction (out of plane).

another. Fig. 20 (f) and (g) show the ends of the left-hand and right-hand cracks, respectively. In each case, the cracks are shown to terminate exactly at the end of the respective twin features. The left-hand crack resulted in the formation of several slip traces and cross-slip at its tip. The right-hand crack tip also coincides with where the twin connects with a grain boundary. Overall, an important observation is that each hydrided twin crack is shown to propagate through the twinned region, as opposed to cracking facilitated by matrix-hydride decohesion. For improved understanding of this detrimental failure mechanism, which was not previously reported, post-deformation EBSD analysis is used in two locations (shown here in Fig. 21 and Fig. 22) to reveal the crack location with respect to the underlying microstructure.

Fig. 21 presents phase and orientation maps of a section of the crack between regions 2 and 3 (referring to Fig. 20 (b)). The phase map shows that the crack effectively only traverses hydrides, i.e., has no interaction with the zirconium matrix. Interestingly, since only the matrix grain orientation is detected, this indicates that the twin has been entirely subsumed by hydride precipitation. The same is true of the EBSD data presented in Fig. 22 (which is of the right-hand crack, marginally below region 5). The data in Fig. 21 show that the full set of four δ hydride orientation variants are detected (two sets of two variants each corresponding to the matrix

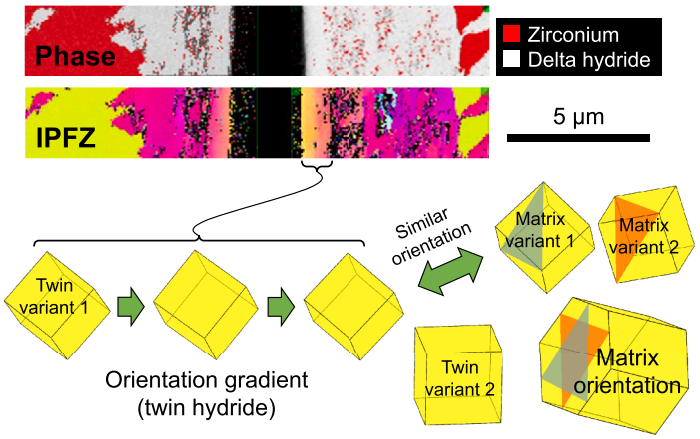

Fig. 21. EBSD phase and orientation data around a crack (between locations 2 and 3 from Fig. 20 (b)) in sample H3. The twin region is shown to have been completely subsumed by hydride precipitation. Four hydride orientations have been identified: two primary grain (matrix) variants and two variants corresponding to the twin (for which orientation data is unavailable).

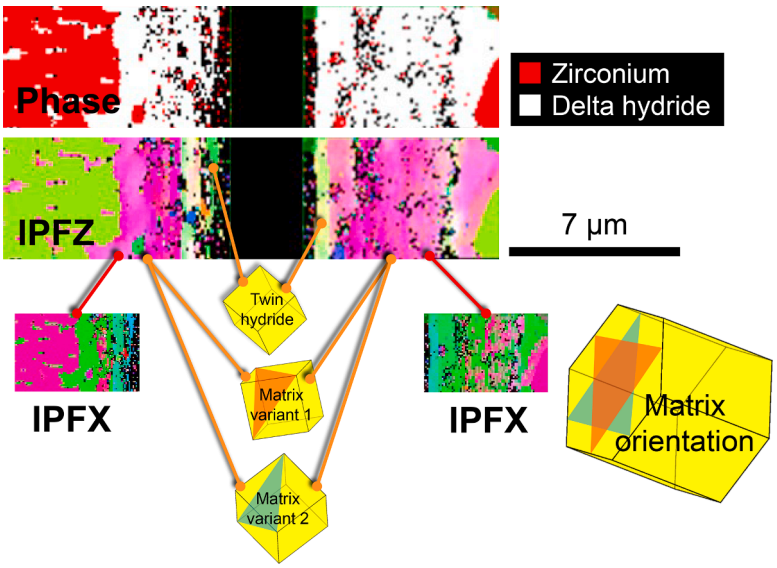

Fig. 22. EBSD phase and orientation data around a crack (along crack path below region 5 from Fig. 20(b)) in sample H3. As in the previously indexed region, the twin orientation is unidentifiable due to being fully hydrided. Matrix hydride variants are identified, as well as a single twin hydride orientation.

grain and matrix twin orientations). Moreover, this important data reveals that both crack interfaces (either side of the crack) are lined by twin hydride variants, demonstrating that the crack is therefore propagating through the centre of the former twin region, rather than at the twin hydride-matrix hydride interface. This is also shown by the second EBSD dataset in Fig. 22, for which there is just a single detectable twin hydride orientation variant, which appears as turquoise in the x-direction inverse pole figure (IPF) orientation maps. The matrix hydride orientation variants are represented by green and pink in the IPFX maps, which show that both variants are roughly equally represented in the typical boundary hydride manner (Wang et al., 2019). Interestingly, the IPFZ map in Fig. 21 shows that there is a very clear hydride orientation gradient at either side of the crack. The gradient varies from an apparent twin orientation at the crack face to an orientation which is close to one of the matrix variants, and is likely to have developed during precipitation. The orientation gradient may also be indicative of the release of energy originally stored in lattice curvature, i.e., GND structure.

The consistency and rate with which cracks are shown to propagate though multiple distinct hydrided twin features indicate that there is some unifying mechanism responsible for this behaviour which has not yet discussed in the literature. Hence, based on the data and observations discussed earlier, a hypothesis for the mechanism is proposed here. As outlined in Fig. 23, for a section of material consisting of a twin sandwiched between two sections of its matrix grain, the chemical potential along either twin-grain interface

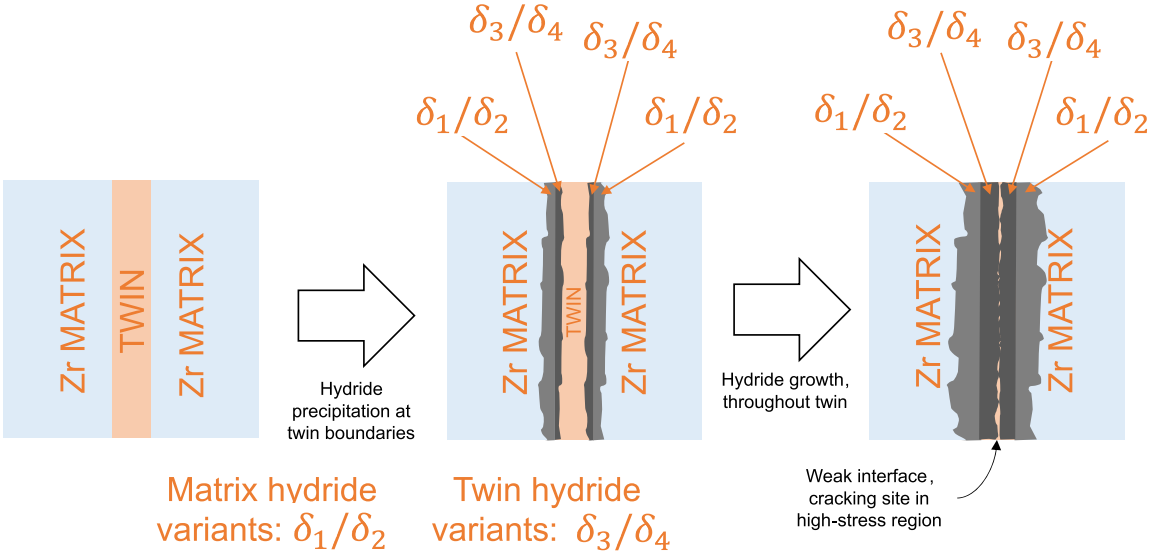

Fig. 23. Hypothesis for crack propagation mechanism linked with formation of hydrides through twin features.

should be equal and be low enough to preferentially sequester mobile hydrogen atoms from the surrounding region at elevated temperatures. During cooling, the onset of hydride precipitation should therefore occur simultaneously along the opposing interfaces which contain the highest levels of hydrogen. As illustrated in Fig. 23, hydride growth could then occur in up to four directions, i.e., along chemical potential gradients, resulting in inward twin hydride growth (variants δ_3 and/or δ_4) from either direction, and outward grain/matrix hydride growth (variants δ_1 and/or δ_2) in each direction.

Hence, the hypothesis proposed here is that at the centre of a twin which has undergone full hydride precipitation, there is some interface/region between hydrides which nucleated at either side of the twin. Owing to the non-uniform rate of hydride growth (as demonstrated by the undulating hydride-matrix interfaces in Fig. 21 and Fig. 22), the interface at the centre of the twin is also likely to be non-uniform, potentially consisting of packets of non-hydrided zirconium. This, in combination with the volumetric expansion associated with hydride precipitation is likely to lead to highly localised deformation (which is also suggested by localised lattice rotation shown in Fig. 21) and decohesion at the centre of the twin prior to the application of any external load, producing a severely weakened interface which is susceptible to cracking under the appropriate conditions. To verify this hypothesis, further work will be required to assess the post-precipitation deformation state using advanced characterisation.

3.4. Implications for cladding performance in commercial nuclear reactors

This study highlights the critical impact of hydride precipitation and strain localisation on the integrity of zirconium-based alloys used in nuclear fuel cladding. The pronounced strain localization at hydride interfaces and the cyclic strain ratcheting observed under thermomechanical loading underscore the importance of understanding hydride behaviour to prevent premature failure. For commercial nuclear power applications, it is recommended to optimise operational protocols to minimise hydride reprecipitation and associated localised strain. Incorporating advanced crystal plasticity modelling that accounts for hydride plasticity and realistic morphologies can enhance predictions of cladding behaviour under service conditions, though hydride plasticity is yet to be incorporated. Additionally, exploring cladding materials with tailored microstructures or compositions to control hydride morphology could significantly improve performance, particularly for the control of crack propagation. More importantly, large grains which may develop at welded connections should be strictly controlled or monitored due to the tendency for hydrides to precipitate along perfectly straight paths within and around twins. These findings can be used to develop approaches which mitigate hydride-related damage and enhance fuel reliability, thereby extending reactor uptime, and ensuring operational safety in commercial nuclear power plants.

4. Conclusions

Under cyclic thermomechanical loads with in situ DIC, the effects of intragranular and intergranular hydride precipitation have been quantified in hydrided Zircaloy-4 with hydrogen contents of 200 ppmw. Single cycle DIC-based residual strain measurements around a newly formed intragranular hydride stringer revealed substantial precipitation strain orientation dependence. Specifically, the in-plane normal strain measured orthogonally to the stringer (along the HCP c-axis direction) was around 4 % within the hydride, whereas virtually no strain was measured in the direction parallel to the stringer. CPFE-based 1D and 2D representations of precipitation of the same hydride revealed that the hydride's morphology was responsible for this effect. After subsequent thermomechanical cycles, hydride strain ratcheting effects were quantified for the first time using DIC, which also revealed the cyclic development of bands of substantial compressive strain within the surrounding matrix. This was shown to lead to the development of GND networks. Intragranular strain ratcheting was shown to saturate after five thermomechanical cycles. Room temperature FCG and cyclic thermomechanical tests were also carried out in hydrided Zircaloy-4 samples. These studies provided new mechanistic insights into how hydrides affect crack propagation mechanisms and ultimately, FCG rates. A variety of crack propagation mechanisms were observed at different length-scales: crystallographic slip-driven crack growth, fatigue cracking along matrix hydride interfaces, and decohesion at these interfaces. Crack growth rate trends are more stochastic in hydrided samples due to added complexity, but intragranular rates were found to be higher, which is potentially linked with facet formation and coalescence between nano-scale hydrides. It was demonstrated that grain boundary hydrides can reduce FCG rates due to strain field diffusion linked with crack branching, etc. It was also demonstrated that in samples containing large twin features, hydride precipitation within and around twins was common. Under cyclic loads, cracks which propagated into hydrided twins resulted in immediate and detrimental sample failure, leading to a new hydride formation-based hypothesis for this previously unreported failure mechanism.

CRediT authorship contribution statement

Daniel J. Long: Writing – original draft, Visualization, Methodology, Investigation, Formal analysis, Conceptualization. **Thibaut Dessolier:** Resources, Conceptualization. **T. Ben Britton:** Writing – review & editing, Resources, Methodology. **Stella Pedrazzini:** Writing – review & editing, Supervision, Resources. **Fionn P.E. Dunne:** Writing – review & editing, Supervision, Resources, Project administration, Methodology, Funding acquisition, Conceptualization.

Declaration of competing interest

The authors declare that they have no known competing financial interests or personal relationships that could have appeared to influence the work reported in this paper.

Acknowledgements

The authors wish to acknowledge the Engineering and Physical Sciences Research Council and Rolls-Royce plc. for their financial contributions to this research work. The authors also acknowledge funding through the MIDAS programme grant (EP/L016273/1). DJL and FPED would also like to express gratitude to Rolls-Royce plc. for their advice relating to the experimental work presented in this paper.

Appendix A. Development of a heat treatment methodology for hydride redistribution

In an experimental laboratory setting, it is difficult to reproduce the conditions which result in engineering component failure, primarily for pragmatic reasons, such as time constraints. In this work, notch defects are introduced artificially to represent naturally occurring surface defects due to e.g., manufacture, in-service oxidation, or hydride blistering. However, since notches were machined prior to the introduction of hydrogen, unwanted interactions between the surface of the notch (due to residual stress) and hydrogen in solution can occur. This effect was reported by Garlea et al. (2010). For isothermal FCG studies, this is not a major concern since the propagating crack quickly extends to a point at which its growth is independent of any such effects. For combined thermal and mechanical loading however, hydride-notch effects can be highly problematic, as illustrated in Fig. A1. At the beginning of a trial thermomechanical fatigue test, while synchronously increasing the temperature and stress, it quickly became clear that the hydrogen content local to the notch was extremely high due to near-immediate hydride stress reorientation.

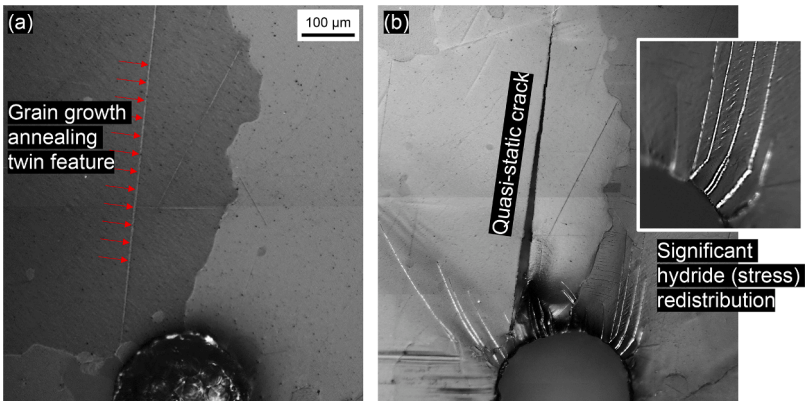

Fig. A1. Detrimental effect of notch, twin features, and hydride presence under monotonic thermomechanical loading. (a) Hydrided microstructure (sample H4) with large twin prior to loading. (b) Same microstructure (H4) after synchronous thermal and mechanical monotonic loading, showing large quasi-static crack which was propagated along or through the twin feature. Substantial hydride reorientation is also shown within the notch due to high initial hydrogen content local to the notch.

This was followed by substantial quasi-static cracking along the twin feature, shown prior to testing in Fig. A1 (a) (throughout which hydrides had precipitated). Hence, prior to achieving even a single thermomechanical fatigue cycle, the sample failed catastrophically due to unwanted and artificial hydride interactions, as shown in Fig. A1 (b). In a previous attempt to counteract these effects, Honniball et al. (2021) quoted a method by which the hydride distribution throughout a sample can be altered prior to testing, while ensuring that meaningful results are maintained. The method involves applying a thermal gradient heat treatment across notched and hydrided zirconium alloy samples (like those used here). Having been originally developed by Canadian Nuclear Laboratories, details of the equipment used were not provided by Honniball et al. (2021); only process details were given, i.e., set temperatures at either end of the sample and heat treatment time. Hence, this appendix describes the design of a thermal gradient heat treatment device for this purpose.

The Soret effect (thermophoresis) is exploited by application of a thermal gradient across a hydrided Zircaloy-4 sample to 'drive' hydrogen away from the notch (for hydrogen in a zirconium lattice, it is driven from high to low temperature regions). Experimentalists at Canadian Nuclear Laboratories found that the optimal high and low temperature boundary conditions (surface temperatures) were 340 °C and 20 – 30 °C, respectively (note that samples were approximately 70 % larger than those used in this chapter). Hence, the heat treatment device developed for the current paper utilises a cartridge heater (mounted within an aluminium block which is attached to a square aluminium contact plate) to heat one face of a sample, while the opposing face is cooled continuously via direct contact with a water-cooled heat sink (see Fig. A2). Contact is maintained between the sample faces and the hot and cold ends using M3 × 40 bolts at each corner of the upper and lower aluminium plates. To mitigate against thermal stresses, springs are added to each bolt, allowing for thermal expansion, as shown in Fig. A2 (c). A 200 W cartridge heater, which can reach temperatures of up to 400 °C is selected to ensure that the high surface temperature can be maintained given the required substantial thermal gradient (approx. 100 °C/mm), i.e., heat transfer rate.

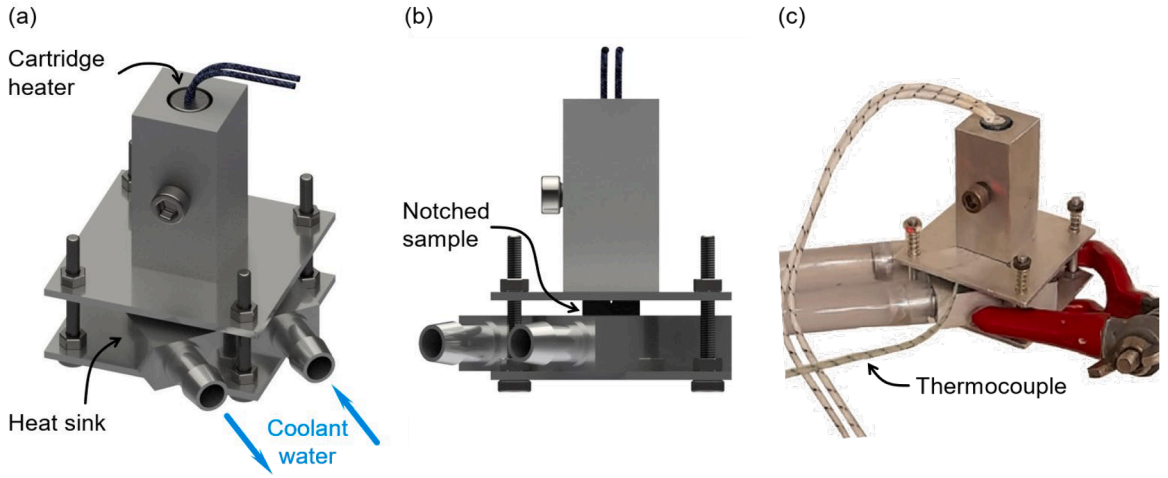

Fig. A2. Design and implementation of thermal gradient heat treatment device. (a) Isometric view of design showing water-cooled heat sink, which is housed between two aluminium plates. The top plate is bolted to an aluminium block, which houses a 200 W cartridge heater (heating element). (b) Side elevation of device showing placement of notched beam sample. The notched end (face) is held in contact with the hot side, while the opposing face is in contact with the heat sink. (c) Actual image of heat treatment unit. Springs are added to the connecting bolts on the hot side to allow for thermal expansion while maintaining sample surface contact. A thermocouple is connected to the hot side aluminium plate, near the sample for temperature control.

For precise temperature control at the hot side, a *Eurotherm 2416* controller is used to control the cartridge heater power via a simple switching algorithm, based on live temperature measurements from a thermocouple mounted to the plate. Due to the substantial cooling rate however, the system takes several minutes to achieve temperature stability, at which point the switching frequency remains very high, resulting in cartridge heater damage and failure (on average, a new heating element was required after heat treatment of every second sample). It is therefore recommended that for future designs of such devices, a custom power control unit be included for constant power steady-state temperature control. At the time of testing, the mains water supply used to cool the heat sink was at around 15 °C. During steady-state operation, the surface temperature of the heat sink (close to the sample) was measured using a separate thermocouple at between 26 and 28 °C, which is within Honniball *et al.*'s recommended range (Honniball et al., 2021).

Despite using the same temperature boundary conditions as those previously reported (Honniball et al., 2021), it is anticipated that the required heat treatment time will be reduced due to a reduced sample size. To generate a hydride denuded region spanning 30 % of the sample thickness, Honniball et al. (2021) applied the thermal gradient heat treatment for 150 h. To estimate the heat treatment time required for the current work, a simple 1D spatial and transient analysis of hydrogen transport is carried out based on the competition of temperature gradient (Soret) and concentration gradient (Fick) effects. Hence, the constitutive equation used to predict the pointwise transient evolution of hydrogen concentration, C, is given by the spatial gradient of hydrogen flux as,

$$\frac{\partial C}{\partial t} = -\nabla(J_{\text{Fick}} + J_{\text{Soret}}) \tag{A1}$$

where J_{Fick} and J_{Soret} are the fluxes due to concentration gradient and temperature gradient, respectively. It is important to note that the current model is only used to estimate an appropriate heat treatment time based on hydrogen transport, and disregards the effects of hydride precipitation and dissolution, etc. Hence the resultant through-thickness hydrogen distributions will be indicative but inaccurate. Fick's law is a function of the diffusion coefficient, D, and concentration gradient as follows,

$$J_{\text{Fick}} = -D\nabla C = -D_0 \exp\left(\frac{Q_{\text{D}}}{RT}\right)\nabla C \tag{A2}$$

where D_0 is the diffusion constant (taken here as 7.9×10^{-7} m^2/s (Lee and Lee, 2023)), and Q_{D} the energy for hydrogen transport in zirconium (taken here as 44,900 J/mol (Lee and Lee, 2023)), and R the universal gas constant. The Soret flux is given by the following equation,

$$J_{\text{Soret}} = -\frac{Q^* DC}{RT^2}\nabla T \tag{A3}$$

where Q^* is the "heat of transport". Based on experimental hydrogen pick-up measurements from Kammenzind et al. (1996), this is taken as 31,000 J/mol. Hence, using Eq. (A1), the updated hydrogen content at position x (between the hot and cold surfaces) after some time increment, Δt is given by Eq. (A4).

$$C(x, t_{i+1}) = C(x, t_i) + \frac{\partial C(t_{i+1})}{\partial t}\Delta t \tag{A4}$$

At the boundaries (hot and cold surfaces, which are represented here as points), the total hydrogen flux is set to zero throughout the simulation, as shown in Fig. A3. Since the hydrogen flux is dependent upon temperature and concentration gradients, and the hydrogen concentration dependent upon flux gradients, it is necessary to embed at least two layers of discretisation, i.e., fluxes are calculated at uniform intervals between either sample face, and hydrogen concentrations and temperatures are calculated and defined at uniform intervals between neighbouring flux calculation points. This is illustrated more clearly in Fig. A3.

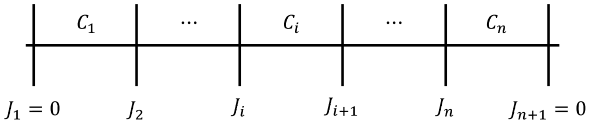

Fig. A3. Illustration showing boundary conditions and method used to calculate hydrogen concentration distribution throughout sample, i.e., since concentration is a function of flux gradients, gradients are easily established between two points by linear interpolation.

Assuming immediate stabilisation of the predefined temperature gradient, the transient and spatial evolution of hydrogen is modelled using a custom *Matlab* script. The results of this are presented for a 3 mm thick sample with a constant thermal gradient for up to 200 h in Fig. A4. Fig. A4 (a) shows the predicted spatial distributions of hydrogen at various stages of heat treatment. At the hot end, most hydrogen redistribution is predicted to occur within the first 10 h of heat treatment; this is most clear in Fig. A4 (b), which shows effective saturation after about 100 h.

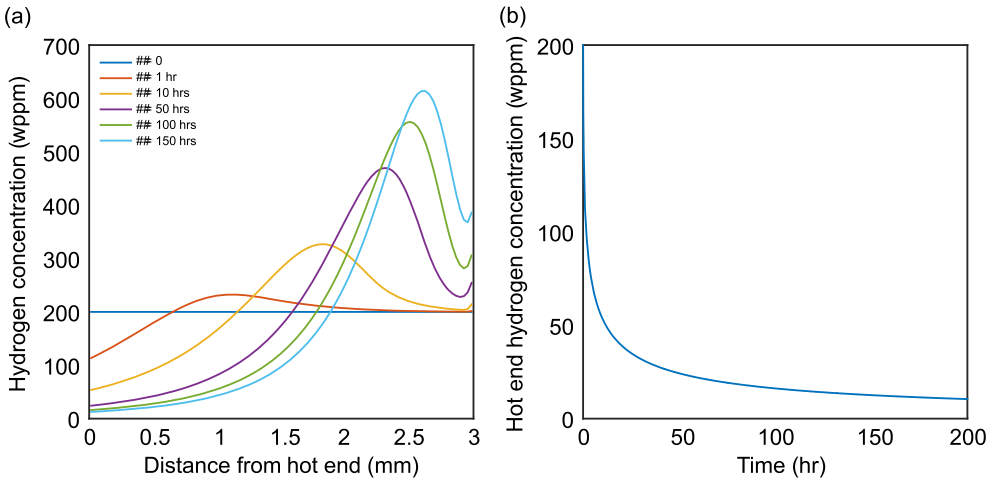

Fig. A4. Influence of heat treatment time on hydrogen distribution. (a) Predicted distribution of hydrogen (at various points in time) between the hot and cold ends of a sample. (b) Predicted evolution of hot end hydrogen content over time.

Fig. A4 (a) also shows that after 100 h of heat treatment, there is a reduced level of hydrogen variation, spatially, between the hot end and the notch tip (which is approx. 300 μm from the hot end). Hence to reduce sample preparation time, a 100-hour heat treatment time is selected for this application.

Upon application of the thermal gradient heat treatment to an otherwise fully prepared sample (sample H1, which underwent a grain growth heat treatment, electrolytic hydrogen charging, and subsequent homogenisation heat treatment, as described in previously), it is necessary to evaluate its effectiveness prior to thermomechanical testing. Fig. A5 shows optical micrographs throughout sample H1 prior to and after the heat treatment. Fig. A5 (a) shows that prior to heat treatment, there is a reasonably uniform distribution of hydrides, with clear evidence of intragranular, intergranular, and twin boundary hydride precipitation. At the upper left-hand edge of the notch, there also appears to be substantial hydride precipitation.

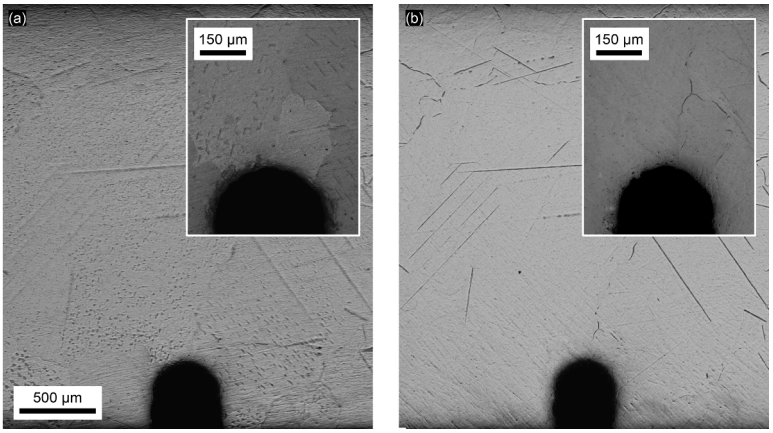

Fig. A5. Hydride distribution throughout sample H1 (a) prior to and (b) after application of thermal gradient heat treatment.

Fig. A5 (b) shows that after the 100-hour thermal gradient heat treatment, there is significant redistribution of hydrides. Firstly, it is immediately clear that throughout the sample, there is a substantial reduction of intragranular hydride fraction, which appears to have resulted in increased precipitation along grain and twin boundaries, as indicated by darkening of these regions. This is unsurprising, since the relatively long-term heat treatment (> 10 times longer than the hydride homogenisation heat treatment) allows ample time for hydrogen transport to these more energetically favourable sites (Alekseeva et al., 2017). More importantly however, the desired non-uniform hydride distribution is attained; specifically, between the lower (hot) end of the sample and the notch tip, virtually no hydrides are visible. Moreover, the hydrides which were observed to precipitate around the upper left-hand edge of the notch are shown to have been removed from this region. Immediately ahead of the notch, there is still clearly grain boundary hydride precipitation, but this is unlikely to produce any unwanted effects during thermomechanical testing.

Data availability

Data will be made available on request.

References

Abdolvand, H., 2019. Progressive modelling and experimentation of hydrogen diffusion and precipitation in anisotropic polycrystals. Int. J. Plast. 116, 39–61. https://doi.org/10.1016/j.ijplas.2018.12.005. May.

Alekseeva, S., et al., 2017. Grain boundary mediated hydriding phase transformations in individual polycrystalline metal nanoparticles. Nat. Commun. 8 (1), 1084. https://doi.org/10.1038/s41467-017-00879-9. Oct.

Ashby, M.F., 1970. The deformation of plastically non-homogeneous materials. Philos. Mag.: J. Theor. Exp. Appl. Phys. 21 (170), 399–424. https://doi.org/10.1080/14786437008238426. Feb.

R. Bigger et al., "A good practices guide for digital image correlation," Oct. 2018. doi: 10.32720/idics/gpg.ed1.

Birch, R., Wang, S., Tong, V.S., Britton, T.B., 2019. The effect of cooling rate and grain size on hydride microstructure in Zircaloy-4. J. Nucl. Mater. 513, 221–225. https://doi.org/10.1016/j.jnucmat.2018.11.011.

Birch, R.M., Douglas, J.O., Britton, T.Ben, 2023. Characterization of local deformation around hydrides in Zircaloy-4 using conventional and high angular resolution electron backscatter diffraction. Mater. Charact. 202, 112988. https://doi.org/10.1016/j.matchar.2023.112988. Aug.

Carpenter, G.J.C., 1973. The dilatational misfit of zirconium hydrides precipitated in zirconium. J. Nucl. Mater. 48 (3), 264–266. https://doi.org/10.1016/0022-3115(73)90022-6. Oct.

Chen, G., Xu, C., Qu, H., Chen, X., 2017. Ratcheting behavior of zirconium alloy tubes under combined cyclic axial load and internal pressure at 350°C. J. Nucl. Mater. 491, 138–148. https://doi.org/10.1016/j.jnucmat.2017.05.006. Aug.

Cockeram, B.V., Kammenzind, B.F., 2018. The increase in fatigue crack growth rates observed for Zircaloy-4 in a PWR environment. J. Nucl. Mater. 499, 111–125. https://doi.org/10.1016/j.jnucmat.2017.11.015. Feb.

Cuniberti, A., Picasso, A., 2001. Activation volume measurement techniques: application to Zircaloy-4. Phys. Status Solidi Appl. Res. 183 (2), 373–379. https://doi.org/10.1002/1521-396X(200102)183:2<373::AID-PSSA373>3.0.CO;2-N. Feb.

Derep, J.L., Ibrahim, S., Rouby, R., Fantozzi, G., 1980. Deformation behaviour of Zircaloy-4 between 77 and 900 K. Acta Metall. 28 (5), 607–619. https://doi.org/10.1016/0001-6160(80)90127-3.

Dunne, F.P.E., Rugg, D., Walker, A., 2007. Lengthscale-dependent, elastically anisotropic, physically-based hcp crystal plasticity: application to cold-dwell fatigue in Ti alloys. Int. J. Plast. 23 (6), 1061–1083. https://doi.org/10.1016/j.ijplas.2006.10.013.

Dunne, F.P.E., Walker, A., Rugg, D., 2007. A systematic study of hcp crystal orientation and morphology effects in polycrystal deformation and fatigue. Proc. R. Soc. A: Math. Phys. Eng. Sci. 463 (2082), 1467–1489. https://doi.org/10.1098/rspa.2007.1833. Jun.

Eadie, R.L., Metzger, D.R., Léger, M., 1993. The thermal ratchetting of hydrogen in zirconium-niobium — an illustration using finite element modelling. Scr. Metall. Mater. 29 (3), 335–340. https://doi.org/10.1016/0956-716X(93)90509-Q. Aug.

Fang, N., Birch, R., Britton, T.Ben, 2022. Optimizing broad ion beam polishing of zircaloy-4 for electron backscatter diffraction analysis. Micron 159, 103268. https://doi.org/10.1016/j.micron.2022.103268.

Farrell, K., Byun, T.S., Hashimoto, N., 2004. Deformation mode maps for tensile deformation of neutron-irradiated structural alloys. J. Nucl. Mater. 335 (3), 471–486. https://doi.org/10.1016/j.jnucmat.2004.08.006. Dec.

Fisher, E.S., Renken, C.J., 1964. Single-crystal elastic moduli and the hcp - bcc transformation in Ti, Zr, and Hf. Phys. Rev. 135 (2A), A482–A494. https://doi.org/10.1103/PhysRev.135.A482. Jul.

Fleck, N.A., Hutchinson, J.W., 1993. A phenomenological theory for strain gradient effects in plasticity. J. Mech. Phys. Solids. 41 (12), 1825–1857.
Garlea, E., et al., 2010. Hydride-phase formation and its influence on fatigue crack propagation behavior in a Zircaloy-4 alloy. Metall. Mater. Trans. A 41 (11), 2816–2828. https://doi.org/10.1007/s11661-010-0342-z. Nov.
Gibbs, G.B., 1964. The thermodynamics of creep deformation. Phys. Status Solidi (b) 5 (3), 693–696. https://doi.org/10.1002/pssb.19640050323.
Gong, J., Benjamin Britton, T., Cuddihy, M.A., Dunne, F.P.E., Wilkinson, A.J., 2015. (a) Prismatic, (a) basal, and (c+a) slip strengths of commercially pure Zr by micro-cantilever tests. Acta Mater. 96, 249–257. https://doi.org/10.1016/j.actamat.2015.06.020.
Hong, J.-D., Yang, Y.-S., Kook, D., 2020. Improvement of delayed hydride cracking assessment of PWR spent fuel during dry storage. Nucl. Eng. Technol. 52 (3), 614–620. https://doi.org/10.1016/j.net.2019.07.036. Mar.
Honniball, P.D., Cogez, L., Gee, C.F., 2021. Influence of hydrides upon the fatigue initiation behavior of irradiated Zircaloy-2. In: Zirconium in the Nuclear Industry: 19th International Symposium. ASTM International, pp. 365–384. https://doi.org/10.1520/stp162220190026.
Huang, J.H., Jiang, F.I., 1994. Cracking of a hydrided zirconium alloy in hydrogen. Hydrogen Effects in Materials. Wiley, pp. 445–454. https://doi.org/10.1002/9781118803363.ch39.
Jiang, J., Zhang, T., Dunne, F.P.E., Britton, T.Ben, 2016. Deformation compatibility in a single crystalline Ni superalloy. Proc. R. Soc. A: Math. Phys. Eng. Sci. 472 (2185), 20150690. https://doi.org/10.1098/rspa.2015.0690. Jan.
Jones, C., et al., 2021. Evidence of hydrogen trapping at second phase particles in zirconium alloys. Sci. Rep. 11 (1), 4370. https://doi.org/10.1038/s41598-021-83859-w. Feb.
Blaber, J., Adair, B., Antoniou, A., 2015. Ncorr: open-source 2D digital image correlation matlab software. Exp Mech 55, 1105–1122. https://doi.org/10.1007/s11340-015-0009-1.
B.F. Kammenzind, D.G. Franklin, W.J. Duffin, and H.R. Peters, "Hydrogen pickup and redistribution in alpha-annealed Zircaloy-4," West Mifflin, PA, Jun. 1996. doi: 10.2172/244661.
M. Kerr, "Mechanical characterization of zirconium hydrides with high energy X-ray diffraction," *Ph.D Thesis*, p. 230, 2009, [Online]. Available: https://ui.adsabs.harvard.edu/abs/2009PhDT.....261K.
Kerr, M., Daymond, M.R., Holt, R.A., Almer, J.D., 2008. Strain evolution of zirconium hydride embedded in a Zircaloy-2 matrix. J. Nucl. Mater. 380 (1–3), 70–75. https://doi.org/10.1016/j.jnucmat.2008.07.004. Oct.
Khan, I.A., Cocks, A.C.F., Chattopadhyay, J., 2021. A study of hydride precipitation in zirconium. Mech. Mater. 155 (January), 103773. https://doi.org/10.1016/j.mechmat.2021.103773.
Kim, Y.S., Kim, K.S., Cheong, Y.M., 2006. Delayed hydride crack velocity of zirconium alloys with the direction of an approach to temperature. J. Nucl. Sci. Technol. 43 (9), 1120–1127. https://doi.org/10.1080/18811248.2006.9711203. Sep.
Laplanche, G., Bonneville, J., Varvenne, C., Curtin, W.A., George, E.P., 2018. Thermal activation parameters of plastic flow reveal deformation mechanisms in the CrMnFeCoNi high-entropy alloy. Acta Mater. 143, 257–264. https://doi.org/10.1016/j.actamat.2017.10.014. Jan.
Lee, C., Lee, Y., 2023. Simulation of hydrogen diffusion along the axial direction in zirconium cladding tube during dry storage. J. Nucl. Mater. 579. https://doi.org/10.1016/j.jnucmat.2023.154352. Jun.
E.H. Lee and D.T. Liu, "Finite strain elastic-plastic theory," in *Irreversible Aspects of Continuum Mechanics and Transfer of Physical Characteristics in Moving Fluids*, H. Parkus and L. I. Sedov, Eds., Vienna: Springer Vienna, 1968, pp. 213–222.
A.D. Lepage, W.A. Ferris, and G.A. Ledoux, "Procedure for adding hydrogen to small sections of zirconium alloys," 1998.
Li, H., Wen, M., Chen, G., Yu, W., Chen, X., 2013. Constitutive modeling for the anisotropic uniaxial ratcheting behavior of Zircaloy-4 alloy at room temperature. J. Nucl. Mater. 443 (1–3), 152–160. https://doi.org/10.1016/j.jnucmat.2013.06.052. Nov.
Li, J., et al., 2019. Effect of hydride precipitation on the fatigue cracking behavior in a zirconium alloy cladding tube. Int. J. Fatigue 129, 105230. https://doi.org/10.1016/j.ijfatigue.2019.105230. Dec.
Li, J., et al., 2022. Uncovering the hydride orientation-mediated hoop fatigue mechanism in a zirconium alloy cladding tube. Int. J. Plast. 159, 103440. https://doi.org/10.1016/j.ijplas.2022.103440. Dec.
Liu, Y., El Chamaa, S., Wenman, M.R., Davies, C.M., Dunne, F.P.E., 2021. Hydrogen concentration and hydrides in Zircaloy-4 during cyclic thermomechanical loading. Acta Mater. 221. https://doi.org/10.1016/j.actamat.2021.117368. Dec.
Liu, Y., Thomas, R., Hardie, C.D., Frankel, P., Dunne, F.P.E., 2023. Exploring the hydride-slip interaction in zirconium alloys. Acta Mater. 261, 119388. https://doi.org/10.1016/j.actamat.2023.119388. Dec.
Y. Liu, W. Wan, S. El Chamaa, M.R. Wenman, C.M. Davies, and F.P.E. Dunne, "Creep and strain rate sensitivity in textured polycrystal Zr alloys (Submitted)," 2020.
Long, D.J., Dunne, F.P.E., 2023. On the mechanistic driving force for short fatigue crack path. J. Mech. Phys. Solids. 179, 105368. https://doi.org/10.1016/j.jmps.2023.105368. Oct.
Long, D.J., Liu, Y., Hardie, C., Dunne, F.P.E., 2024. Synergistic coupling of thermomechanical loading and irradiation damage in Zircaloy-4. Model. Simul. Mat. Sci. Eng. 32 (4), 045007. https://doi.org/10.1088/1361-651X/ad312b. Jun.
Long, D.J., Wan, W., Dunne, F.P.E., 2022. The influence of microstructure on short fatigue crack growth rates in Zircaloy-4: crystal plasticity modelling and experiment. Int. J. Fatigue, 107385. https://doi.org/10.1016/j.ijfatigue.2022.107385. Feb.
Massih, A.R., Jernkvist, L.O., 2021. Solid state phase transformation kinetics in Zr-base alloys. Sci. Rep. 11 (1), 7022. https://doi.org/10.1038/s41598-021-86308-w. Mar.
McNamara, F., 2014. Hydrides in Zirconium Alloys. PhD Thesis. Imperial College London, London.
Olsson, P.A.T., Massih, A.R., Blomqvist, J., Alvarez Holston, A.-M., Bjerkén, C., 2014. Ab initio thermodynamics of zirconium hydrides and deuterides. Comput. Mater. Sci. 86, 211–222. https://doi.org/10.1016/j.commatsci.2014.01.043. Apr.
Perovic, V., Weatherly, G.C., Simpson, C.J., 1983. Hydride precipitation in α/β zirconium alloys. Acta Metall. 31 (9), 1381–1391.
Poole, B.O., 2020. Deformation Mechanisms in Iron-Base Hard Facing Alloys. Imperial College London, London.
Radu, V., Roth, M., 2012. Probabilistic fracture mechanics applied for DHC assessment in the cool-down transients for CANDU pressure tubes. Nucl. Eng. Des. 253, 211–218. https://doi.org/10.1016/j.nucengdes.2012.08.036. Dec.
Sunil, S., Gopalan, A., Bind, A.K., Sharma, R.K., Murty, T.N., Singh, R.N., 2020. Effect of radial hydride on delayed hydride cracking behaviour of Zr-2.5Nb pressure tube material. J. Nucl. Mater. 542, 152457. https://doi.org/10.1016/j.jnucmat.2020.152457. Dec.
Taherijam, M., Marashi, S., Tondro, A., Abdolvand, H., 2023. On the effects of transformation strain induced by hydride precipitation. Acta Mater. 261, 119356. https://doi.org/10.1016/j.actamat.2023.119356. Dec.
Taylor, G.I., 1934. The mechanism of plastic deformation of crystals. Part I. Theoretical. Proc. R. Soc. Lond., Contain. Pap. Math. Phys. Character 145 (855), 362–387 [Online]. Available. http://www.jstor.org/stable/2935509.
Tong, V.S., 2016. EBSD Characterisation of Heterogeneous Microstructures in Zirconium Alloys. Imperial College London, London.
Wan, W., Dunne, F.P.E., 2020. Microstructure-interacting short crack growth in blocky alpha Zircaloy-4. Int. J. Plast. 130 (February), 102711. https://doi.org/10.1016/j.ijplas.2020.102711.
Wang, S., Giuliani, F., Britton, T.Ben, 2019. Variable temperature micropillar compression to reveal <a> basal slip properties of Zircaloy-4. Scr. Mater. 162, 451–455. https://doi.org/10.1016/j.scriptamat.2018.12.014. Mar.
Wang, S., Giuliani, F., Britton, T.Ben, 2019. Microstructure and formation mechanisms of δ-hydrides in variable grain size Zircaloy-4 studied by electron backscatter diffraction. Acta Mater. 169, 76–87. https://doi.org/10.1016/j.actamat.2019.02.042. May.
Wanhill, R.J.H., Ryder, D.A., Davies, T.J., 1972. Metallographic studies of fatigue in 20% cold-worked zircaloy-2 containing zirconium hydride. J. Nucl. Mater. 43 (2), 75–85. https://doi.org/10.1016/0022-3115(72)90141-9. May.
Weekes, H.E., Jones, N.G., Lindley, T.C., Dye, D., 2016. Hydride reorientation in Zircaloy-4 examined by in situ synchrotron X-ray diffraction. J. Nucl. Mater. 478, 32–41. https://doi.org/10.1016/j.jnucmat.2016.05.029.

Xu, Y., Wan, W., Dunne, F.P.E., 2021. Microstructural fracture mechanics: stored energy density at fatigue cracks. J. Mech. Phys. Solids. 146, 104209. https://doi.org/10.1016/j.jmps.2020.104209. August 2020.

Zan, X.D., Guo, X., Weng, G.J., 2024. Hydride-enhanced strain localization in zirconium alloy: a study by crystal plasticity finite element method. Int. J. Plast. 174, 103911. https://doi.org/10.1016/j.ijplas.2024.103911. Mar.

Zeng, X., Zhang, C., Zhu, W., Zhu, M., Wang, Y., Zhang, X., 2022. Quantitative characterization of short fatigue crack and grain boundary interaction behavior in zirconium. Int. J. Fatigue 161. https://doi.org/10.1016/j.ijfatigue.2022.106894. Aug.

Zhang, Y., You, L., Li, X., Zhou, J., Song, X., 2020. In-situ investigation of the fatigue crack initiation and propagation behavior of Zircaloy-4 with different hydrogen contents at RT and 300°C. J. Nucl. Mater. 532, 152065. https://doi.org/10.1016/j.jnucmat.2020.152065. Apr.